Atmos. Chem. Phys. Discuss., 12, 3983–4029, 2012
www.atmos-chem-phys-discuss.net/12/3983/2012/
doi:10.5194/acpd-12-3983-2012

Atmospheric Chemistry and Physics Discussions

MAX-DOAS measurements of NO_2, HCHO and CHOCHO at a rural site in Southern China

X. Li[1,2], T. Brauers[2], A. Hofzumahaus[2], K. Lu[1,2], Y. P. Li[1,2], M. Shao[1], T. Wagner[3], and A. Wahner[2]

[1]College of Environmental Sciences and Engineering, Peking University, Beijing, China
[2]Institut für Energie- und Klimaforschung Troposphäre (IEK-8), Forschungszentrum Jülich, Jülich, Germany
[3]Max-Planck-Institut für Chemie, Mainz, Germany

Received: 12 January 2012 – Accepted: 23 January 2012 – Published: 3 February 2012

Correspondence to: T. Brauers (th.brauers@fz-juelich.de)

Published by Copernicus Publications on behalf of the European Geosciences Union.

Abstract

We performed MAX-DOAS measurements during the PRIDE-PRD2006 campaign in the Pearl River Delta region (PRD), China, for 4 weeks in July 2006 at a site located 60 km north of Guangzhou. The vertical distributions of NO_2, HCHO, and CHOCHO were independently retrieved by an automated iteration method. The MAX-DOAS measured NO_2 mixing ratios showed reasonable agreement with the simultaneous, ground based in-situ data. While the tropospheric NO_2 vertical column densities (VCDs) observed by OMI on board EOS-Aura satellite agreed with those by MAX-DOAS, the 3-D chemical transport model CMAQ overestimated the NO_2 VCDs as well as the surface concentrations by about 40 %. From this observation, a reduction of NO_x emission strength in CMAQ seems to be necessary in order to well reproduce the NO_2 observations. The average mixing ratios of HCHO and CHOCHO were 12 ppb and 1.6 ppb, respectively, substantially higher than in other rural or semirural environments. The high ratio of 0.135 between CHOCHO and HCHO corresponds to the high VOCs reactivity and high HO_x turnover rate consistent with other observations during the campaign.

1 Introduction

Multi-axis differential optical absorption spectroscopy (MAX-DOAS) is a novel and effective remote sensing method for measuring tropospheric trace gases such as SO_2, HCHO, NO_2, CHOCHO (Irie et al., 2011; Wagner et al., 2011, and references therein). MAX-DOAS uses scattered sunlight at different elevation angles α (i.e. the angle between horizon and the pointing direction of the telescope). The slant column density (SCD), which is the concentration of a species integrated along the paths where the registered photons traveled, can be derived from a DOAS fit. Despite the simplicity of the experimental setup, the conversion from measured SCDs to trace gas concentrations or profiles is a demanding task. As illustrated in Table 1, along with the numerous MAX-DOAS applications in the past decades, different methodologies for deriving the

ACPD

12, 3983–4029, 2012

MAX-DOAS trace gases measurements in China

X. Li et al.

Title Page

Abstract | Introduction

Conclusions | References

Tables | Figures

◀| |▶

◀ ▶

Back | Close

Full Screen / Esc

Printer-friendly Version

Interactive Discussion

trace gas concentrations have been developed. The geometric approach, which is based on the assumption that a photon was scattered only once before it reaches the telescope, was used for estimating the trace gas concentrations in remote areas (Leser et al., 2003). However, for MAX-DOAS observations in the UV or at high aerosol loads the single scattering assumption is not valid. Under these conditions, radiative transfer models (RTMs) are required to derive trace gas profiles from measured SCDs. The different RTMs (see Table 1) calculate SCDs for trace gases on the basis of trace gas profiles as input to the model. In order to optimize the model input an inversion method is needed. This can either be optimal estimation (Rodgers, 2000) or an iteration procedure as presented by Pikelnaya et al. (2007). Both algorithms consist of two steps, i.e. first the aerosol extinction profile is retrieved from the measured oxygen dimer (O_4) absorptions, then the trace gas profile is retrieved from the measured trace gas absorptions taking the aerosol extinction profile into account. Given the routinely MAX-DOAS measurements often generate large data sets, an automated inversion method (e.g., Irie et al., 2011) is highly preferable. Inherently, only 2–3 independent pieces of profile information can be retrieved from the MAX-DOAS measurements. Therefore, during the inversion process, either a-priori information on the profile needs to be provided or a profile parameterization needs to be applied based on assumptions of the profile shape. Recent studies have compared the MAX-DOAS measured trace gas (e.g. NO_2, HCHO) concentrations in the boundary layer to those obtained by in-situ techniques. In general, the differences were within 30 % (Pikelnaya et al., 2007; Inomata et al., 2008; Irie et al., 2011; Wagner et al., 2011). In addition, MAX-DOAS can serve as a tool to validate satellite-borne trace gas observations. The differences between MAX-DOAS and satellite measured NO_2 tropospheric vertical column densities were found to be 10–50 % for selected regions (Irie et al., 2008; Brinksma et al., 2008; Boersma et al., 2009).

With the fast economic growth, the air quality has been of increasing concern in the Pearl River Delta (PRD) region in Southern China. In the last years, PRD was identified by satellite measurements as one of the "hot-spots" of NO_2, HCHO, and

ACPD
12, 3983–4029, 2012

CHOCHO (Richter et al., 2005; Wittrock et al., 2006; Vrekoussis et al., 2009). The observed high NO_2 levels reflect the prevailing anthropogenic emission sources, e.g. vehicles and industrial sources. Since HCHO and CHOCHO are mainly produced through the oxidation of volatile organic compounds (VOCs), their high concentration levels indicate the large photochemical turnover in the PRD atmosphere. However, only a few ground-based HCHO and CHOCHO measurements were reported for this region. During the PRIDE-PRD2006 field campaign, we performed one month of continuous MAX-DOAS observations for O_4, NO_2, HCHO, and CHOCHO. An automated aerosol retrieval method using O_4 absorption was developed, and the retrieved aerosol extinction agreed well with the total aerosol scattering measured by a nephelometer (Li et al., 2010). Here, we present the retrieval method and results for NO_2, HCHO, and CHOCHO concentrations. These results are discussed with respect to simultaneously measured in-situ data, satellite observations, and chemical transport model simulations.

2 Experimental

2.1 Field campaign and measurement site

The PRIDE-PRD2006 field campaign took place in July 2006 in the Pearl River Delta (PRD) region in Southern China within the framework of the "Program of Regional Integrated Experiments of Air Quality over the Pearl River Delta" (PRIDE-PRD2006). The campaign focused on photochemistry and the formation of secondary pollutants like ozone and particles (Zhang et al., 2012). The MAX-DOAS measurements were conducted at one of the campaign supersites Back Garden (BG) located 23.50° N and 113.03° E. The BG site is approximately 60 km NW of downtown Guangzhou. It is located next to a water reservoir and is surrounded by farmland and small forests. During the campaign, the local traffic was quite limited. However, road works, building constructions, and biomass and cable burning were occasionally observed in the

ACPD
12, 3983–4029, 2012

surrounding areas. The biomass and cable burning events were intense and prevailing in the period between 23 July and 25 July leading to high concentrations of aerosols and trace gases (Garland et al., 2008; Lou et al., 2010). The entire campaign was characterized by tropical weather conditions with high temperatures (28–36 °C) and high humidities (60–95 % RH). Extended rainfall occurred in periods influenced by typhoons Bilis (15–18 July) and Kaemi (26–29 July). The wind speed at BG site was usually low (less than $2\,m\,s^{-1}$) in most of the time, which is a typical situation for inland areas in PRD during summer time (Fan et al., 2011). Such meteorological conditions favors the formation and accumulation of air pollution. High OH radical concentrations with noontime peak values of $(1.5–2.6) \times 10^7\,cm^{-3}$ as well as high OH reactivities k_{OH} with values between $20\,s^{-1}$ and $120\,s^{-1}$ were observed at the BG site during the campaign (Lou et al., 2010; Lu et al., 2011). These observations indicate a strong photochemical processing compared to those in other places in the world.

A comprehensive suit of instruments was simultaneously operated at the BG supersite for the characterization of trace gases (Hua et al., 2008; Hofzumahaus et al., 2009; Lou et al., 2010; Lu et al., 2011; Li et al., 2011) and aerosols (Garland et al., 2008; Li et al., 2010; Yue et al., 2010; Xiao et al., 2011) in the local atmosphere. Measurements of NO_X, O_3, SO_2, H_2O_2, CO, CH_4, C3-C12 VOCs, CH_3OOH, HCHO, CHOCHO, aerosol physical and chemical properties, and photolysis frequencies were performed on top of a hotel building (10 m a.g.l.) which was exclusively used by the measurement team. OH, HO_2, HONO, and OH reactivities were measured on top of a two stacked sea containers located about 200 m away from the hotel building. Detailed information with respect to the instrumentations, the accuracy and precision of the measurements can be found in Hofzumahaus et al. (2009), Yue et al. (2010), and Li et al. (2011).

2.2 MAX-DOAS

Our MAX-DOAS measurements were conducted by a commercial Mini-MAX-DOAS instrument (Fa. Hoffmann, Rauenberg, Germany). Since the instrument setup was described in detail by Li et al. (2010), only a brief outline follows. The Mini-MAX-DOAS instrument was installed on top of the hotel building, pointing East. It uses a miniature crossed Czerny-Turner spectrometer unit USB2000 (Ocean Optics Inc.) for spectrum sampling. The spectrometer covers the spectral range of 292 nm to 443 nm with a spectral resolution of ≈ 0.7 nm full width at half maximum (FWHM). The scattered sunlight was collected and focused by a quartz lens and was led into the spectrometer unit by a quartz fiber bundle. A step motor was used for adjusting the viewing direction to a desired elevation angle α, i.e. 90°, 30°, 20°, 15°, 10°, 5°, and 3°. During daytime, one measurement cycle consisted of the sequential record of the scattered sunlight spectrum at the seven elevation angles and took 10–15 min. For each spectrum, a constant signal level (i.e. 80 % of the saturation of the detector) was achieved by adjusting the integration time. During night, the instrument was set to record dark current and offset spectra. A fully automated program (MiniMax, Udo Friess, University of Heidelberg) was employed for the MAX-DOAS measurements.

The differential slant column density (DSCD) is defined as the difference of the slant column density (SCD) between $\alpha \neq 90°$ and $\alpha = 90°$ (c.f. Wagner et al., 2011). DSCDs of NO_2, HCHO, and CHOCHO were determined by DOAS fit in the wavelength range where they have prominent absorptions. Figure 1 illustrates an example of the DOAS fit for the spectrum recorded on 19 July 2006 at 10:59, at a solar zenith angle of 23° and an elevation angle of 3°. For each measurement cycle, the corresponding zenith spectrum ($\alpha = 90°$) was taken as Fraunhofer reference spectrum (FRS) for the off-axis elevation angles (i.e. $\alpha \neq 90°$). This largely eliminates the stratospheric contributions to the DSCDs. The Ring spectrum was calculated from each measured spectrum (Bussemer, 1993). For the fit of the absorbing trace gases, we used high resolution absorption cross sections which were convolved with the instrument slit function to match the resolution of the instrument (except for O_4 spectrum which was interpolated). These references include HCHO (Meller and Moortgat, 2000), BrO (Wilmouth et al., 1999), CHOCHO (Volkamer et al., 2005), H_2O (Rothman et al., 2005), NO_2 (Voigt et al., 2002), O_3 at 280 K (Voigt et al., 2001), and O_4 (Greenblatt et al., 1990) with a manual adjustments of wavelength axis (R. Sinreich, personal communication, 2007). In addition, the

ACPD
12, 3983–4029, 2012

solar I_0-effect (Platt et al., 1997) was corrected for NO_2 and O_3 reference spectra with slant column density of 1.5×10^{17} cm^{-2} and 1.5×10^{20} cm^{-2}, respectively. The wavelength calibration was performed by fitting the Fraunhofer reference spectra to a high resolution Fraunhofer spectrum (Kurucz et al., 1984), convoluted with the instrument's slit function.

The conversion from measured DSCDs to tropospheric vertical column density (VCD) is usually done by the differential air mass factor (DAMF). The air mass factor (AMF) can be regarded as the path enhancement of SCD compared to VCD. DAMF is defined as the the difference of air mass factor (AMF) between $\alpha \neq 90^\circ$ and $\alpha = 90^\circ$. If the last scattering event of photons been registered by the MAX-DOAS telescope happens above the trace gas layer, the AMF for the zenith and the off-axis view can be estimated as 1 and $1/\sin\alpha$, respectively. Thus, the trace gas tropospheric VCD can be written as

$$VCD_{geo} = \frac{DSCD_\alpha}{DAMF_\alpha} = \frac{DSCD_\alpha}{(1/\sin\alpha) - 1} \quad (1)$$

where α is the elevation angle of the telescope. This method is called "geometric approach". For photons received by the telescope at higher elevation angles, the probability of their last scattering event occurring above the trace gas layer is increased. Thus we calculated VCD_{geo} for NO_2, HCHO, and CHOCHO from the corresponding DSCDs at the highest off-zenith elevation angle, i.e. $\alpha = 30^\circ$.

Compared to the simple geometric approach, the radiative transfer transfer modeling of DSCDs is a demanding task. In this study, the DSCDs calculations were performed by McArtim, which is a backward Monte-Carlo RTM with the treatment of multiple scattering in a fully spherical geometry (Deutschmann et al., 2011). For each trace gas (NO_2, HCHO, and CHOCHO), its vertical distribution was retrieved by iteratively adjusting the profile until the measured DSCDs best fit with the modeled DSCDs. The parameter settings of McArtim are listed in Table 2. Following Li et al. (2010), we used a two-layer setup for the trace gas distribution in the troposphere (0–15 km height). The trace gas concentrations (unit: cm^{-3}) were assumed to be homogeneous

ACPD
12, 3983–4029, 2012

in a layer near the ground surface (called mixed layer, ML), while the concentrations in the layer aloft (i.e. the free troposphere) decrease exponentially with height. This type of trace gas distribution was frequently observed in polluted regions (e.g., Fried et al., 2003; Junkermann, 2009; Klippel et al., 2011). The concentration profile $c(z)$ can be described with a limited set of parameters

$$c(z) = \begin{cases} \mathrm{VCD} \cdot F/H & z \leq H \\ \beta \cdot \exp(-z/\xi) & z > H \end{cases} \tag{2}$$

where z is the height above ground, VCD denotes the trace gas tropospheric vertical column density of the respective trace gas, F is the fraction of the $\mathrm{VCD}_{\mathrm{rtm}}$ residing in the ML, and H is the height of ML. β is the norm for exponential factor and ξ is the scaling height for the trace gas in the free troposphere. We performed test runs of the retrieval and we found that the results were not sensitive to ξ under these conditions encountered here since most of the trace gases were present in the mixed layer. Thus ξ was set to a constant value of 5 km. The norm β is calculated from the integral of $c(z)$ over the entire troposphere $\mathrm{VCD} = \int_{0\,\mathrm{km}}^{15\,\mathrm{km}} c(z)dz$ leading to

$$\beta = \frac{(1-F) \cdot \mathrm{VCD}}{\xi(\exp(-H/\xi) - \exp(-15\,\mathrm{km}/\xi))} \tag{3}$$

With the input given above, the McArtim program calculates the set of trace gas DSCDs (R_α) at the six elevation angles of the measurements. In order to achieve the best estimates for F, H, $\mathrm{VCD}_{\mathrm{rtm}}$ (subscript rtm refers to the use of the RTM, in contrast to the geometric approach) we minimized

$$\chi^2(\mathrm{VCD}_{\mathrm{rtm}}, F, H) = \sum_{\alpha=3^\circ}^{30^\circ} \left(\frac{M_\alpha - R_\alpha(\mathrm{VCD}_{\mathrm{rtm}}, F, H)}{\sigma(M_\alpha)} \right)^2 \tag{4}$$

where M_α represents the measured DSCDs. The weights are presented by the statistical error (precision) of the measured data, $\sigma(M_\alpha)$. In order to reduce the atmospheric variations as well as measurement noise of a single observation, the profile

ACPD
12, 3983–4029, 2012

retrieval was applied for measured DSCDs averaged over one hour. The minimization procedure was conducted automatically using an implementation of the Levenberg-Marquardt algorithm (mpfit[1], realized in IDL).

Since the PRD region is characterized by wide spread emission sources, most of the trace gases reside in the ML and the trace gas concentrations in the ML are much higher than those in the layer aloft. Therefore, the modeled DSCDs are not sensitive to change of ξ (see above), and values of F are close to 1. The three parameter (VCD_{rtm}, F, and H) retrieval yielded $F > 0.95$ for almost all cloud-free periods. In addition, the statistical error of the retrieved F was large associated with a cross-correlation between F and H. Increasing H or decreasing F have the same effect on the modeled DSCDs. In order to overcome this issue, we finally fixed the values of F to 1; only VCD and H were retrieved. This approach resulted in a "box shape" profile. The trace gas concentrations c_0 are universal in the box and equal to VCD_{rtm}/H. c_0 can then be compared to ground-based measurements which were done at the BG site.

Figure 2 depicts the flow diagram of the trace gas vertical distribution retrieval procedure. In order to well simulate the aerosol scattering effects by RTM, aerosol vertical distributions were retrieved beforehand from O_4 DSCDs in the way as described by Li et al. (2010). The derived aerosol extinction profiles were used as input to the trace gas vertical distribution retrieval. The retrieval of NO_2 vertical distribution was performed as the second step. Using the results from the first two steps, HCHO and CHOCHO vertical distributions were retrieved independently.

The errors of the retrieved trace gas vertical distribution consist of statistical errors which arise mainly from the uncertainty of the DSCDs, and systematic errors which originate from the uncertainty of the RTM input parameters and of the DSCD simulation. The statistical errors were derived from the mpfit procedure. Within RTM intercomparison activities (Hendrick et al., 2006; Wagner et al., 2007) the uncertainty of DSCD calculations by McArtim were found to be less than 10 %. The sensitivities

[1]C. B. Markwardt, mpfit – Robust non-linear least squares curve fitting, http://cow.physics.wisc.edu/~craigm/idl/fitting.html.

ACPD
12, 3983–4029, 2012

of the modeled DCSDs with respect to RTM input parameters are listed in Table 3. The surface albedo, the field of view of the telescope (FOV), and the surface O_3 and NO_2 have minor influences on the modeled DSCDs. The major uncertainty sources to the modeled DSCDs are the aerosol properties, namely the single scattering albedo (SSA), the asymmetry factor (g, under the Henyey-Greenstein approximation), and the aerosol optical depth (AOD). While the increase of SSA and g lead to a simultaneous increase of modeled DSCDs at all elevation angles, the increase of AOD results in a decrease of modeled DSCDs. It was found that 30 % change of modeled DSCDs results in ≈ 25 % change of the retrieved VCD_{rtm} and c_0. During the campaign, the systematic errors of the measured SSA and AOD were 10 % and 30 %, respectively, and the uncertainty of g was 10 % (Garland et al., 2008; Li et al., 2010). Therefore, we conclude that the total systematic error of the retrieved VCD_{rtm} and c_0 are around 35 %.

2.3 In-situ NO_2 measurement

In-situ NO_2 concentrations were measured by a commercial instrument (Takegawa et al., 2006). The inlet of the sampling line was located on top of the hotel building. NO_2 in the sampled air was converted to NO in a photolytical reactor (Droplet Measurement Technologies, Model BLC) with an conversion efficiency of 30 %. The NO was then detected by NO-O_3 chemiluminescence (Thermo Electron, Model 42CTL). The 1 min detection limit for NO_2 was 170 ppt, and the corresponding accuracy was 13 %.

2.4 Numerical simulation of NO_2

Model3-CMAQ version 4.5.1 was employed to simulate the NO_2 concentrations during the period of the campaign. Details of the model configuration are described by Wang et al. (2010). The CMAQ model uses SAPRC99 as chemical mechanism, and is driven by MM5 for meteorology field and SMOKE for source emissions. The time step of the model was set to 1 h. There are three nested domains in the model system with

ACPD
12, 3983–4029, 2012

grid spacing of 36 km, 12 km, and 4 km. All grids have 13 layers vertically extending from the surface to an altitude of 17 km above the ground, with seven layers below 1 km and the first layer thickness of 18 m. While the TRACE-P anthropogenic emission inventory was used for the 36 km domain, the emission inventories used for the 12 km domain and the 4 km domain were updated according to recent studies in PRD region (Zheng et al., 2009). Mobile sources and power generation point sources contribute about 47 % and 39 %, respectively, to the total NO_X emissions in PRD while mobile sources, evaporation losses of solvents and petroleum, and biogenic sources are the three largest contributors to VOC emissions, accounting for 38 %, 24 %, and 23 %, respectively. Spatially, both NO_X and VOC emissions are concentrated over the inland urban areas of Guangzhou, Foshan, and Dongguan; the coastal areas of Dongguan and Shenzhen; and the urban core of Hong Kong.

3 Results

The MAX-DOAS instrument was operated for the campaign period from 3 July to 25 July 2006. However, as already discussed by Li et al. (2010), only 9 virtually cloud-free days were suitable for aerosol and trace gas vertical distribution retrieval. Measured DSCDs of NO_2, HCHO, and CHOCHO in these 9 days are displayed in Fig. S1 in the Supplement.

The vertical column densities using the RTM retrieval (VCD_{rtm}) of NO_2, HCHO, and CHOCHO are shown in Figs. 3–5. The mean values of VCD_{rtm} were 1.0×10^{16} cm^{-2}, 2.9×10^{16} cm^{-2}, and 3.5×10^{15} cm^{-2} for NO_2, HCHO, and CHOCHO, respectively. VCD_{rtm} of NO_2 and HCHO showed the same diurnal variation pattern; higher values were usually observed around early morning before 09:00 LT (local time, LT = UTC + 8 h) and late afternoon (after 17:00 LT). Besides 23 July, peak values of CHOCHO VCD_{rtm} occurred in the afternoon (12:00–15:00 LT). Considering the measurement and retrieval errors, VCDs calculated by the geometric approach (VCD_{geo}) are nearly identical with the VCD_{rtm}. For the whole data set ($N = 109$), the slopes B_0

ACPD
12, 3983–4029, 2012

of a linear regression forced trough the origin (VCD_{geo} versus VCD_{rtm}) are 1.06 ± 0.14 ($R^2 = 0.97$) for NO_2, 1.05 ± 0.07 ($R^2 = 0.80$) for HCHO, and 1.00 ± 0.07 ($R^2 = 0.60$) for CHOCHO, respectively (Figs. S2–S4).

The retrieved mixed layer heights H of the three trace gases are shown in Fig. 6. H_{NO_2}, H_{HCHO}, and H_{CHOCHO} are not always the same. In early morning hours, when H_{NO_2} and H_{CHOCHO} were below 200 m, H_{HCHO} was in the range of 300 m to 1 km. H_{CHOCHO} increased dramatically during the day and reached peak values of 2–4 km in the afternoon. The maxima of H_{NO_2} coincided with that of H_{CHOCHO}, however, the maximum values of H_{NO_2} were only 1–2 km. Compared to H_{NO_2} and H_{CHOCHO}, the diurnal variation of H_{HCHO} was less prominent. In some days (e.g. 24 July), peak values of H_{HCHO} around 2 km can be clearly identified in the afternoon. In the other days (e.g. 20 July), H_{HCHO} kept stable at 1 km with variation of ± 200 m.

The trace gas mixing ratios (in ppb) at ground level can be calculated as $m_0 = VCD/H \times M_0$ with M_0 being the conversion factor from cm^{-3} to ppb. Figure 7 shows the time series of the derived NO_2, HCHO, and CHOCHO mixing ratios. The average daytime mixing ratios of NO_2, HCHO, and CHOCHO were 9.5 ppb, 11.8 ppb, and 1.6 ppb, respectively. During the days 23 July–25 July when intense biomass and electric cable burning events occurred in the previous night in the surrounding areas, high levels of HCHO (≈ 40 ppb) and CHOCHO (≈ 6 ppb) were found in the early morning hours. In the same time periods, NO_2 mixing ratios up to 45 ppb were observed by both MAX-DOAS and in-situ techniques and the mixing ratios of NO_2, HCHO, and CHOCHO show similar diurnal pattern having their maxima in the early morning hours. With the increase of solar radiation, mixed layer height, and OH concentration, all mixing ratios started to decrease after 09:00 LT and became stable in the afternoon. A slight increase of m_0 can be found before sunset. While the mixing ratio of NO_2 and HCHO varied in the similar way as their VCDs during the day, the variation of the CHOCHO mixing ratio was opposite to the CHOCHO VCDs.

ACPD
12, 3983–4029, 2012

4 Discussion

4.1 NO_2

The good agreement between NO_2 VCD_{rtm} and NO_2 VCD_{geo} (Figs. 3 and S1) indicates that the geometric approach is well suited for estimating the tropospheric NO_2 VCDs at the BG site, even given the high aerosol loads during the campaign (Garland et al., 2008; Li et al., 2010). Similar results were found by Wagner et al. (2011) in the Po Valley area, i.e. differences between NO_2 VCD_{geo} and VCD_{rtm} were within 12 %. However, different to Wagner et al. (2011), we did not observe a dependence of the relative difference between VCD_{rtm} and VCD_{geo} ($\Delta VCD = (VCD_{rtm} - VCD_{geo})/VCD_{rtm}$) on the mixed layer height (H_{NO_2}) at the BG site; ΔVCD and H_{NO_2} are uncorrelated ($R^2 = 0.02$). Since the differences between VCD_{geo} and VCD_{rtm} are rather small and in the order of the measurement and data retrieval uncertainties, no correlation between ΔVCD and other measured parameters can be expected.

Simultaneous in-situ NO_2 measurements can be used to validate the NO_2 mixing ratios derived from the MAX-DOAS observations. The scatter plot of NO_2 mixing ratios derived from MAX-DOAS vs. in-situ chemiluminescence data (Fig. 10) provides a high degree of correlation, $R^2 = 0.81$ for a data set of $N = 107$ simultaneous measurements. However, at this high degree of correlation, the slope B_0, forced through the origin, is 1.35 ± 0.21. Considering the errors in both coordinates, the goodness-of-fit parameter Q (cf. Press et al., 2007) equals 0.9 indicating that the scatter of the data points around the regression line can be explained by the measurement errors of both techniques. Here we included the fit error (usually small) and the errors of the SSA, g, and AOD, since these can vary with the different conditions during the campaign.

However, the 35 % difference between MAX-DOAS and the in-situ technique is slightly larger than the obtained by Pikelnaya et al. (2007); Irie et al. (2008); Wagner et al. (2011) where differences of 30 % or less were observed. Firstly, we investigated if the 35 % difference can be attributed to the inhomogeneous distribution of NO_2 along the lines of the previous studies. During the campaign, the NO_X emission usually occurred in the second half of the night or in the early morning. However, the relative difference of NO_2 mixing ratios between the two techniques (i.e. ΔVCD) correlates neither with the time of the day ($R^2 = 0.01$), nor with the NO_2 layer height ($R^2 = 0$), nor the wind speed ($R^2 = 0.03$), suggesting the emission or transport effects, which can result in the imhomogenity of NO_2 distribution, have minor influence on the intercomparison results in this study. Secondly, we investigated if the higher NO_2 mixing ratios observed by MAX-DOAS can be attributed to the uncertainty of parameters used in the RTM calculation. As discussed in Sect. 2.2, the aerosol properties, namely SSA, g, and AOD, are the major contributors to the systematic error of the MAX-DOAS NO_2 retrieval. In the RTM calculation, SSA was fixed to the measured average value 0.85 and we assumed g to be constant at 0.68. However, due to the change of aerosol compositions and size distributions, the values of SSA and g change. Using the RTM we performed a number of sensitivity studies showing that an increase of SSA and g lead to higher values of modeled NO_2 DSCDs and higher retrieved NO_2 mixing ratios. Although the AOD and the aerosol vertical distribution used in the RTM calculation were derived from the MAX-DOAS observations, they are sensititve to the values of SSA and g (Li et al., 2010). During the campaign, the uncertainty of SSA, g, and AOD were 10 %, 10 %, and 30 %, respectively, which can lead to an uncertainty of ≈ 25 % for the retrieved NO_2 mixing ratios. In addition, the uncertainty of the RTM DSCDs simulation contributes another 10 % systematic error and the accuracy of the in-situ NO_2 measurements was 13 %. Therefore, the 35 % difference between the NO_2 mixing ratios observed by MAX-DOAS and by the in-situ technique are within the range provided by the systematic errors and the error of the slope. The difference observed here is substantially lower than in the studies by Celarier et al. (2008) and Chen et al. (2009) who did not use the locally measured aerosol and NO_2 profiles.

The ground-based MAX-DOAS observations can also be used as an effective way for the validation of trace gas VCDs derived from satellite measurements, since both methods are based on the DOAS technique but differ in the viewing directions (i.e.

ACPD
12, 3983–4029, 2012

one looking up to the sky, the other looking down to the earth). Here, we compared the tropospheric NO_2 VCDs measured by MAX-DOAS and by OMI (Ozone Monitoring Instrument on board NASA's EOS-Aura satellite) for the BG site during the PRIDE-PRD2006 campaign. The OMI tropospheric vertical column densities of NO_2 (VCD_{omi}) were downloaded from http://www.temis.nl (DOMINO Version 2.0). The DOMINO products also include information on cloud fraction (CF). Details on the NO_2 VCD_{omi} and CF retrieval are described by Boersma et al. (2007) with recent updates in the DOMINO Product Specification Document (http://www.temis.nl/docs/OMI_NO2_HE5_1.0.2.pdf). The uncertainties of NO_2 VCD_{omi} and CF are ≈ 30 % and < 5 %, respectively, according to Boersma et al. (2007). Figure S5 shows the time series of NO_2 VCD_{geo}, VCD_{rtm}, and VCD_{omi} during the entire campaign period. Given the ground pixel size of the OMI observation (≥ 340 km^2) and the satellite overpass time (≈ 14:00 LT) the cloud-free days discriminated from our sky-webcam images are only a subset of those by the OMI cloud fraction (i.e. CF ≤ 0.5). The relationship between MAX-DOAS and OMI measured tropospheric NO_2 VCDs is shown in Fig. 9. The NO_2 VCD_{omi} were significantly lower than NO_2 VCD_{geo} when CF > 0.5, which can be expected since OMI only detects the NO_2 absorption above the cloud. When taking all measurement days into account, we found poor correlation ($R^2 = 0.20$) of VCD_{omi} against VCD_{geo} (Fig. 9a). This is mainly caused by the large discrepancy between VCD_{omi} and VCD_{geo} in cloudy days. When we restrict to observations during the virtually cloud-free days, VCD_{omi} were found to agree better with VCD_{geo} ($R^2 = 0.63$; $B_0 = 0.91 \pm 0.20$). Though similar regression slope ($B_0 = 0.97 \pm 0.24$) is obtained when compare VCD_{omi} to VCD_{rtm}, R^2 of 0.49 suggests a weaker relationship between VCD_{omi} and VCD_{rtm} (Fig. 9b). The majority of previous studies demonstrated that the tropospheric NO_2 VCDs measured by OMI were between 10 % and 50% lower than those measured by ground-based instruments, like MAX-DOAS and direct sun measurements (Brinksma et al., 2008; Celarier et al., 2008; Irie et al., 2008; Boersma et al., 2009). In contrast, Halla et al. (2011) observed at a rural site in Southwestern Ontario, that the NO_2 VCDs measured by OMI can be 50 % higher than those derived from MAX-DOAS measurements.

ACPD
12, 3983–4029, 2012

Both, the overestimation and the underestimation were mainly attributed to the inhomogeneous distribution of NO_2 especially for measurements in or near source regions, since OMI observations effectively average the NO_2 concentrations over its field of view ($\geq 340\,km^2$) while the ground-based instruments at a single spot. Therefore, we conclude that the tropospheric NO_2 VCDs measured by OMI are in good agreement with those by MAX-DOAS at the BG site during the cloud-free days of the PRIDE-PRD2006 campaign.

The NO_2 simulations of the CMAQ model were also compared to MAX-DOAS and in-situ measurement at the BG site during the cloud-free days. As shown in Figs. 3 and 8, the modeled NO_2 concentrations follow the observations, but on average they are about 40 % higher than the observed values. The linear regression of VCD_{cmaq} vs. VCD_{rtm} yielded a slope $B_0 = 1.39 \pm 0.17$ while the surface layer NO_2 concentrations of the CMAQ model and the insitu instrument gave $B_0 = 1.38 \pm 0.18$. However, in the morning of 23 July and 24 July, the CMAQ modeled NO_2 VCDs and surface layer concentrations are only 20–40 % of the measured values. This was caused by local emission events (i.e. biomass and electric cable burning) which are not included in the source inventory of the CMAQ model. The occurrence of the local emission events were identified by measurements of aerosol optical properties and OH reactivities at the BG site, as described by Garland et al. (2008) and Lou et al. (2010), respectively. After excluding the data in these periods, the modeled NO_2 concentrations exceed the measured values by 75 % on average. In the CMAQ model, the simulated NO_2 levels are mainly determined by the dilution effects and the NO_X emissions. The dilution effects are related with the wind speed and the vertical mixing. In the morning of 12 July and 19 July, when the modeled wind speeds were quite small and much lower than the local observations (Fig. S6), the accumulation of trace gases in the model can be expected and resulted in the simulated NO_2 concentrations be 3–4 times of the measured values. In other time periods, although the modeled wind speeds were either comparable with or higher than the locally measured values (Fig. S6), which is not in favor of the accumulation of air pollutants, the simulated NO_2 concentrations are still ≈ 55 % higher than the measurement results.

When strong vertical mixing occurs, NO_2 emitted or produced near the ground can be effectively transported to higher altitudes. The strength of the vertical mixing is reflected by the mixed layer height of NO_2 (H_{NO_2}). Figure 8 shows the time series of the NO_2 concentrations modeled by CMAQ in different height ranges. In the early morning (before 07:00 LT) and late afternoon (after 17:00 LT), the modeled NO_2 concentrations in the surface layer ($c^{NO_2}_{0\to 18m}$) were usually 5 times higher than those in the layer of 0–1 km ($c^{NO_2}_{0\to 1\,km}$), indicating that most of the NO_2 was concentrated in a shallow layer above the ground and H_{NO_2} being less than 1 km. After 08:00 LT, the differences between $c^{NO_2}_{0\to 18\,m}$, $c^{NO_2}_{0\to 1\,km}$, and $c^{NO_2}_{0\to 3\,km}$ became smaller, and $c^{NO_2}_{0\to 1\,km}$ nearly equals $c^{NO_2}_{0\to 18\,m}$. suggesting an increase of H_{NO_2} to more than 1 km. The H_{NO_2} estimated from the modeled NO_2 distributions were almost the same as those derived from the MAX-DOAS observations (cf. H_{NO_2} in Fig. 6). Since the CMAQ model can reproduce the observed H_{NO_2}, it is unlikely that the vertical mixing of NO_2 in the model was underestimated. Given the discussion above, we conclude that the dilution effects can not explain the higher modeled NO_2 concentrations than the measurements. In order to obtain better agreement between the modeled and measured NO_2 concentrations reduced NO_X emissions in the source inventory of the CMAQ model seem to be necessary.

4.2 HCHO and CHOCHO

The HCHO and CHOCHO concentrations observed in this work are among the highest ever reported (Table 4), which is consistent with PRD was identified by satellite measurements as one of the hot spot regions of HCHO and CHOCHO (De Smedt et al., 2008; Myriokefalitakis et al., 2008; Vrekoussis et al., 2009). Given HCHO and CHOCHO are mostly produced through the oxidation of different VOCs, their observed high concentrations indicate high levels of the precursor VOCs and the enormous HO_X turnover in the atmosphere of PRD region, which have also been demonstrated by Lou

ACPD
12, 3983–4029, 2012

et al. (2010) and Lu et al. (2011). HCHO and CHOCHO at the BG site showed different diurnal variation than the observations in other places in the world (e.g., Munger et al., 1995; Lei et al., 2009), i.e. the maximum mixing ratios always occurred in early morning hours (Fig. 7) instead of around noon. The early occurrence of HCHO and CHOCHO peaks can be attributed to the oxidation of VOCs by OH radicals in the previous night. During the campaign, nighttime OH concentrations were constantly higher than zero and had an average of $\approx 1 \times 10^6\,cm^{-3}$ (Lu et al., 2011), while the average OH reactivities were 30–50 s^{-1} at night. Therefore, nighttime production of HCHO and CHOCHO are possible under these conditions and in the absence of photolysis, HCHO and CHOCHO can easily accumulate. After sunrise, due to the increase of photolysis frequencies and the mixed layer height, HCHO and CHOCHO mixing ratios started to decrease and became stable in the afternoon.

The mixed layer heights of CHOCHO (H_{CHOCHO}) are higher than those of NO_2 and HCHO especially in the afternoon (Fig. 6). During the campaign, the lifetimes of NO_2, HCHO, and CHOCHO around noon due to reaction with OH and photolysis were calculated to be ≈ 2 min, ≈ 1.4 h, and ≈ 1.2 h, respectively, based on the observed OH concentration of $\approx 1.4 \times 10^7\,cm^{-3}$ and the measured photolysis frequency of $\approx 7 \times 10^{-3}\,s^{-1}$ for NO_2, $\approx 6 \times 10^{-5}\,s^{-1}$ for HCHO and $\approx 9 \times 10^{-5}\,s^{-1}$ for CHOCHO. Due to the short lifetime of NO_2, lower H_{NO_2} than H_{CHOCHO} can be expected. Even though the lifetime of CHOCHO and HCHO were comparable, they are produced in different generations of the VOCs oxidation which can result in different vertical distribution of CHOCHO and HCHO. Imagine an airmass containing primary VOCs being transported from the emission sources to the receptor site. As a first or second generation product, HCHO is produced before CHOCHO which is usually produced from the second or third generation daughter products of primary VOCs. Thus, with the aging of the airmass the production of CHOCHO can proceed. In another words, the maxima of CHOCHO concentration occurs later than that of HCHO. Since the airmass also undergoes vertical mixing the different timing of the production of HCHO and CHOCHO is converted into different vertical extensions. The observed H_{CHOCHO} is likely to be higher than H_{HCHO}.

Both species, CHOCHO and HCHO, are mainly produced through hydrocarbon oxidation. The ratio of CHOCHO to HCHO (R_{GF}) was used in a number of studies to identify the sources of VOCs since CHOCHO and HCHO have different precursors or different formation pathways (e.g., Vrekoussis et al., 2010). Figure 11 shows the diurnal variation of the CHOCHO to HCHO ratio (R_{GF}) in the 9 cloud-free days. Although R_{GF} calculated from the mixing ratio near the ground surface ($R_{GF,m0}$) have similar average value as that from VCD_{rtm} ($R_{GF,m0} = 0.135 \pm 0.069$, $R_{GF,rtm} = 0.177 \pm 0.183$), they show different diurnal variations. While $R_{GF,m0}$ is nearly constant over the day, values of $R_{GF,rtm}$ around noon were higher than that in the morning and late afternoon. This difference is caused by the different variation between the CHOCHO mixing ratio (i.e. m_0) compared to the CHOCHO vertical column densities (i.e. VCD_{rtm}) (Figs. 5 and 7). Since HCHO and CHOCHO VCDs derived from the geometric approach (VCD_{geo}) agree with their VCD_{rtm} (Figs. S3 and S4), good agreement between $R_{GF,geo}$ (i.e. R_{GF} calculated from VCD_{geo}) and $R_{GF,rtm}$ can be expected ($B_0 = 1.02 \pm 0.12$, $R^2 = 0.69$).

Values of R_{GF} depend on many factors including primary emissions, compositions and concentrations of precursor VOCs, OH levels, etc. R_{GF} higher than 0.5 were found by Schauer et al. (2001) in biomass burning emissions, whilst R_{GF} were in the range of 0.02–0.09 in vehicle exhausts (Schauer et al., 1999, 2002). Since different types of VOCs (i.e. alkane, alkene, aromatic, oxygenated VOCs) have different yields of HCHO and CHOCHO, values of R_{GF} can be different when the VOCs compositions change. Moreover, given CHOCHO is usually the higher generation oxidation product of primary VOCs, in the condition of higher HO_X turnover rates, more CHOCHO can be produced leading to higher R_{GF}. Table 4 lists R_{GF} obtained in different environments in the world. In general, R_{GF} in rural areas are below 0.1, whilst values higher than 0.1 exist in urban areas. Besides the lower concentrations of ambient VOCs, most rural areas are strongly influenced by biogenic VOC emissions, e.g. isoprene, terpenes, and 2-methyl-3-butene-2-ol (MBO) (Lee et al., 1995; Munger et al., 1995; Huisman et al., 2011). Compared to anthropogenic VOCs (e.g. aromatics), the CHOCHO yield from isoprene or terpenes oxidations are much lower (Fu et al., 2008). Therefore, though

ACPD
12, 3983–4029, 2012

MAX-DOAS trace gases measurements in China

X. Li et al.

Giesta, Portugal is geologically defined as rural site, the strong influence of anthropogenic emissions from industries in surrounding areas cause high levels of HCHO, CHOCHO, and R_{GF}. On other hand, in urban areas like Sao Paulo, Brazil and Mexico City, Mexico, when primary emission (e.g. traffic) accounts for a large fraction of ambient HCHO but barely contributes to CHOCHO (Grosjean et al., 1990; Lei et al., 2009), the prevailing anthropogenic sources can cause a decrease of R_{GF}. It was also found that, for the same measurement site (i.e. Montelibretti, Italy, Las Vegas, USA, and Elizabeth, USA), R_{GF} obtained in summer are higher than in other seasons (Jing et al., 2001; Liu et al., 2006; Possanzini et al., 2007). This is because summer time is usually accompanied by high solar radiation, temperature, and humidity, which are in favor of the photochemical reactions producing HCHO, CHOCHO, and other secondary products. R_{GF} obtained at the BG site are higher than the values in most rural areas but comparable with those in urban conditions. As described by Lu et al. (2011), during the PRIDE-PRD2006 campaign, the detected air masses were mixtures of anthropogenic and biogenic emissions. Additionally, the observed high OH and k_{OH} level indicate the fast ongoing photochemistry which has rarely been reported for other places in the world. However, in the relationship between R_{GF} and other measured parameters (e.g. NO_X, O_3, VOCs, OH, k_{OH}, OH × k_{OH}), no correlations were found. This is probably due to R_{GF} is determined by the combination of several factors (e.g. the concentration and composition of precursors, the OH level, the photolysis frequencies, etc), which is difficult to be reflected by a single parameter.

The spatial distribution of R_{GF} and its implication on VOC source types have been investigated by Vrekoussis et al. (2010) using satellite measurements. Their observed R_{GF} of ≈ 0.04 for Southern Asia is much lower than the values obtained at the BG site. This difference can be explained by the different spatial resolution between the satellite and local measurements. Vrekoussis et al. (2010) suggest that R_{GF} in the range of 0.04–0.06 can represent regions where biogenic emissions are the dominant primary VOC sources, while values lower than 0.04 indicate elevated anthropogenic VOC emissions. However, referring to Table 4, their suggestion seems only consistent with

ACPD
12, 3983–4029, 2012

the observations for rural areas. The major argument of $R_{GF} < 0.04$ representing regions influenced by anthropogenic emissions is, the primary HCHO from anthropogenic sources can cause a decrease of R_{GF} (Vrekoussis et al., 2010). As discussed above, this is indeed the case for Mexico City, Mexico, but might not always be true for areas where the primary HCHO concentration is low but anthropogenic VOCs (e.g. aromatics) are at high level. According to Table 4, R_{GF} in urban areas are in general higher than 0.04 by a factor of 2. To solve the difference between the conclusion of Vrekoussis et al. (2010) and this study, more simultaneous HCHO and CHOCHO measurements at different locations and seasons are needed. Furthermore, it is necessary to apply the photochemical modeling of HCHO and CHOCHO in terms of VOC compositions.

5 Summary and conclusion

During the PRIDE-PRD2006 campaign in Southern China in July 2006, we performed MAX-DOAS measurements for NO_2, HCHO, and CHOCHO at a rural site 60 km NW of downtown Guangzhou. Under the assumption of a "box profile" setup for the three trace gases, their tropospheric vertical column densities, mixing layer heights, and mixing ratios at the ground have been retrieved by an automated algorithm.

- The simple geometric approach is able to provide good estimates of the NO_2 tropospheric VCDs even under the relatively high aerosol loads encountered here.
- A comparison of OMI tropospheric NO_2 VCDs with our ground-based MAX-DOAS measurements showed a good agreement when the cloud fraction was below 0.5.
- A comparison to the 3-D chemical transport model CMAQ showed a high degree of correlation for NO_2 VCDs and NO_2 ground level concentrations but the model overestimates the measured values indicating a need for a reduction of the NO_X emission strength in the source inventory.

ACPD
12, 3983–4029, 2012

- The HCHO and CHOCHO concentrations and their ratios R_{GF} were much higher than expected from previous studies. This can be attributed to the high photochemical turnover in the PRD region.
- Different from satellite observations, our ground-based measurements indicate that R_{GF} are lower than 0.1 in rural areas but increase with higher anthropogenic emissions.

Based on these findings, simultaneous measurements of HCHO and CHOCHO and their precursors as well as photochemical modeling are necessary in order to obtain a clearer picture on the influence of anthropogenic and biogenic emissions on R_{GF}. We also showed in this case study for NO_2 that MAX-DOAS can serve as an excellent tool for 3-d CTM evaluation and for satellite validation even under specific conditions here. The automated MAX-DOAS retrieval of VCDs and mixed layer heights are a first step towards using MAX-DOAS product for data assimilation forecast models.

Supplementary material related to this article is available online at: http://www.atmos-chem-phys-discuss.net/12/3983/2012/ acpd-12-3983-2012-supplement.pdf.

Acknowledgements. The authors like to thank Roman Sinreich, Udo Frieß, and Ulrich Platt (Heidelberg) for the lending of the Mini-MAX DOAS instrument, the MiniMax software, and fruitful discussions. The technical help and support at the field site from the PRIDE-PRD2006 campaign team, especially Rolf Häseler (Jülich), Min Hu, Limin Zeng, and Yuanhang Zhang (Beijing) are gratefully acknowledged. We thank all participants of the distributed computing of the RTM. We acknowledge the free use of tropospheric NO_2 column data from the OMI sensor from www.temis.nl. This work was supported by the China National Basic Research and Development Program 2002CB410801, and the National High Technology Research and Development Program of China (863 Program) 2006AA06A301.

ACPD
12, 3983–4029, 2012

References

Bobrowski, N., Honninger, G., Galle, B., and Platt, U.: Detection of bromine monoxide in a volcanic plume, Nature, 423, 273–276, doi:10.1038/nature01625, 2003. 4015

Boersma, K. F., Eskes, H. J., Veefkind, J. P., Brinksma, E. J., van der A, R. J., Sneep, M., van den Oord, G. H. J., Levelt, P. F., Stammes, P., Gleason, J. F., and Bucsela, E. J.: Near-real time retrieval of tropospheric NO_2 from OMI, Atmos. Chem. Phys., 7, 2103–2118, doi:10.5194/acp-7-2103-2007, 2007. 3997

Boersma, K. F., Jacob, D. J., Trainic, M., Rudich, Y., DeSmedt, I., Dirksen, R., and Eskes, H. J.: Validation of urban NO_2 concentrations and their diurnal and seasonal variations observed from the SCIAMACHY and OMI sensors using in situ surface measurements in Israeli cities, Atmos. Chem. Phys., 9, 3867–3879, doi:10.5194/acp-9-3867-2009, 2009. 3985, 3997

Borrego, C., Gomes, P., Barros, N., and Miranda, A. I.: Importance of handling organic atmospheric pollutants for assessing air quality, J. Chromatogr. A, 889, 271–279, doi:10.1016/S0021-9673(00)00230-2, 2000. 4018

Brinksma, E. J., Pinardi, G., Volten, H., Braak, R., Richter, A., Schöhardt, A., van Roozendael, M., Fayt, C., Hermans, C., Dirksen, R. J., Vlemmix, T., Berkhout, A. J. C., Swart, D. P. J., Oetjen, H., Wittrock, F., Wagner, T., Ibrahim, O. W., de Leeuw, G., Moerman, M., Curier, R. L., Celarier, E. A., Cede, A., Knap, W. H., Veefkind, J. P., Eskes, H. J., Allaart, M., Rothe, R., Piters, A. J. M., and Levelt, P. F.: The 2005 and 2006 DANDELIONS NO_2 and aerosol intercomparison campaigns, J. Geophys. Res., 113, D16S46, doi:10.1029/2007JD008808, 2008. 3985, 3997

Bussemer, M.: Der Ring-Effekt: Ursachen und Einfluß auf die spektroskopische Messung stratosphäischer Spurenstoffe, Diploma thesis, Universität Heidelberg, Heidelberg, Germany, 1993. 3988

Celarier, E. A., Brinksma, E. J., Gleason, J. F., Veefkind, J. P., Cede, A., Herman, J. R., Ionov, D., Goutail, F., Pommereau, J.-P., Lambert, J.-C., van Roozendael, M., Pinardi, G., Wittrock, F., Schönhardt, A., Richter, A., Ibrahim, O. W., Wagner, T., Bojkov, B., Mount, G., Spinei, E., Chen, C. M., Pongetti, T. J., Sander, S. P., Bucsela, E. J., Wenig, M. O., Swart, D. P. J., Volten, H., Kroon, M., and Levelt, P. F.: Validation of Ozone Monitoring Instrument nitrogen dioxide columns, J. Geophys. Res., 113, D15S15, doi:10.1029/2007JD008908, 2008. 3996, 3997

Cerqueira, M. A., Pio, C. A., Gomes, P. A., Matos, J. S., and Nunes, T. V.: Volatile organic compounds in rural atmospheres of Central Portugal, Sci. Total Environ., 313, 49–60, doi:10.1016/S0048-9697(03)00250-X, 2003. 4018

Chen, D., Zhou, B., Beirle, S., Chen, L. M., and Wagner, T.: Tropospheric NO_2 column densities deduced from zenith-sky DOAS measurements in Shanghai, China, and their application to satellite validation, Atmos. Chem. Phys., 9, 3641–3662, doi:10.5194/acp-9-3641-2009, 2009. 3996

Choi, W., Faloona, I. C., Bouvier-Brown, N. C., McKay, M., Goldstein, A. H., Mao, J., Brune, W. H., LaFranchi, B. W., Cohen, R. C., Wolfe, G. M., Thornton, J. A., Sonnenfroh, D. M., and Millet, D. B.: Observations of elevated formaldehyde over a forest canopy suggest missing sources from rapid oxidation of arboreal hydrocarbons, Atmos. Chem. Phys., 10, 8761–8781, doi:10.5194/acp-10-8761-2010, 2010. 4018

De Smedt, I., Müller, J.-F., Stavrakou, T., van der A, R., Eskes, H., and Van Roozendael, M.: Twelve years of global observations of formaldehyde in the troposphere using GOME and SCIAMACHY sensors, Atmos. Chem. Phys., 8, 4947–4963, doi:10.5194/acp-8-4947-2008, 2008. 3999

Deutschmann, T., Beirle, S., Frieß, U., Grzegorski, M., Kern, C., Kritten, L., Platt, U., Prados-Román, C., Pukite, J., Wagner, T., Werner, B., and Pfeilsticker, K.: The Monte Carlo atmospheric radiative transfer model McArtim: introduction and validation of Jacobians and 3D features, J. Quant. Spectrosc. Ra., 112, 1119–1137, doi:10.1016/j.jqsrt.2010.12.009, 2011. 3989

Fan, S. J., Fan, Q., Yu, W., Luo, X. Y., Wang, B. M., Song, L. L., and Leong, K. L.: Atmospheric boundary layer characteristics over the Pearl River Delta, China, during the summer of 2006: measurement and model results, Atmos. Chem. Phys., 11, 6297–6310, doi:10.5194/acp-11-6297-2011, 2011. 3987

Fried, A., Crawford, J., Olson, J., Walega, J., Potter, W., Wert, B., Jordan, C., Anderson, B., Shetter, R., Lefer, B., Blake, D., Blake, N., Meinardi, S., Heikes, B., O'Sullivan, D., Snow, J., Fuelberg, H., Kiley, C. M., Sandholm, S., Tan, D., Sachse, G., Singh, H., Faloona, I., Harward, C. N., and Carmichael, G. R.: Airborne tunable diode laser measurements of formaldehyde during TRACE-P: distributions and box model comparisons, J. Geophys. Res., 108, 8798, doi:10.1029/2003jd003451, 2003. 3990

Fu, T.-M., Jacob, D. J., Wittrock, F., Burrows, J. P., Vrekoussis, M., and Henze, D. K.: Global budgets of atmospheric glyoxal and methylglyoxal, and implications for formation of secondary organic aerosols, J. Geophys. Res., 113, D15303, doi:10.1029/2007JD009505, 2008. 4001

ACPD
12, 3983–4029, 2012

Garland, R. M., Yang, H., Schmid, O., Rose, D., Nowak, A., Achtert, P., Wiedensohler, A., Takegawa, N., Kita, K., Miyazaki, Y., Kondo, Y., Hu, M., Shao, M., Zeng, L. M., Zhang, Y. H., Andreae, M. O., and Pöschl, U.: Aerosol optical properties in a rural environment near the mega-city Guangzhou, China: implications for regional air pollution, radiative forcing and remote sensing, Atmos. Chem. Phys., 8, 5161–5186, doi:10.5194/acp-8-5161-2008, 2008. 3987, 3992, 3995, 3998

Greenblatt, G. D., Orlando, J. J., Burkholder, J. B., and Ravishankara, A. R.: Absorption measurements of oxygen between 330 and 1140 nm, J. Geophys. Res., 95, 18577–18582, doi:10.1029/JD095iD11p18577, 1990. 3988

Grosjean, D., Miguel, A. H., and Tavares, T. M.: Urban air pollution in Brazil: acetaldehyde and other carbonyls, Atmos. Environ. B-Urb., 24, 101–106, doi:10.1016/0957-1272(90)90015-M, 1990. 4002, 4018

Grosjean, E., Grosjean, D., Fraser, M. P., and Cass, G. R.: Air quality model evaluation data for organics. 2. C_1-C_{14} carbonyls in Los Angeles air, Environ. Sci. Technol., 30, 2687, doi:10.1021/es950758w, 1996. 4018

Halla, J. D., Wagner, T., Beirle, S., Brook, J. R., Hayden, K. L., O'Brien, J. M., Ng, A., Majonis, D., Wenig, M. O., and McLaren, R.: Determination of tropospheric vertical columns of NO_2 and aerosol optical properties in a rural setting using MAX-DOAS, Atmos. Chem. Phys., 11, 12475–12498, doi:10.5194/acp-11-12475-2011, 2011. 3997

Heckel, A., Richter, A., Tarsu, T., Wittrock, F., Hak, C., Pundt, I., Junkermann, W., and Burrows, J. P.: MAX-DOAS measurements of formaldehyde in the Po-Valley, Atmos. Chem. Phys., 5, 909–918, doi:10.5194/acp-5-909-2005, 2005. 4015

Hendrick, F., Van Roozendael, M., Kylling, A., Petritoli, A., Rozanov, A., Sanghavi, S., Schofield, R., von Friedeburg, C., Wagner, T., Wittrock, F., Fonteyn, D., and De Mazière, M.: Intercomparison exercise between different radiative transfer models used for the interpretation of ground-based zenith-sky and multi-axis DOAS observations, Atmos. Chem. Phys., 6, 93–108, doi:10.5194/acp-6-93-2006, 2006. 3991

Ho, S. S. H. and Yu, J. Z.: Feasibility of collection and analysis of airborne carbonyls by on-sorbent derivatization and thermal desorption, Anal. Chem., 74, 1232–1240, doi:10.1021/ac015708q, 2002. 4018

Hofzumahaus, A., Rohrer, F., Lu, K., Bohn, B., Brauers, T., Chang, C.-C., Fuchs, H., Holland, F., Kita, K., Kondo, Y., Li, X., Lou, S., Shao, M., Zeng, L., Wahner, A., and Zhang, Y.: Amplified trace gas removal in the troposphere, Science, 324, 1702–1704,

ACPD
12, 3983–4029, 2012

doi:10.1126/science.1164566, 2009. 3987
Hönninger, G. and Platt, U.: Observations of BrO and its vertical distribution during surface ozone depletion at Alert, Atmos. Environ., 36, 2481–2489, doi:10.1016/S1352-2310(02)00104-8, 2002. 4015
Hua, W., Chen, Z. M., Jie, C. Y., Kondo, Y., Hofzumahaus, A., Takegawa, N., Chang, C. C., Lu, K. D., Miyazaki, Y., Kita, K., Wang, H. L., Zhang, Y. H., and Hu, M.: Atmospheric hydrogen peroxide and organic hydroperoxides during PRIDE-PRD'06, China: their concentration, formation mechanism and contribution to secondary aerosols, Atmos. Chem. Phys., 8, 6755–6773, doi:10.5194/acp-8-6755-2008, 2008. 3987
Huisman, A. J., Hottle, J. R., Galloway, M. M., DiGangi, J. P., Coens, K. L., Choi, W., Faloona, I. C., Gilman, J. B., Kuster, W. C., de Gouw, J., Bouvier-Brown, N. C., Goldstein, A. H., LaFranchi, B. W., Cohen, R. C., Wolfe, G. M., Thornton, J. A., Docherty, K. S., Farmer, D. K., Cubison, M. J., Jimenez, J. L., Mao, J., Brune, W. H., and Keutsch, F. N.: Photochemical modeling of glyoxal at a rural site: observations and analysis from BEARPEX 2007, Atmos. Chem. Phys., 11, 8883–8897, doi:10.5194/acp-11-8883-2011, 2011. 4001, 4018
Inomata, S., Tanimoto, H., Kameyama, S., Tsunogai, U., Irie, H., Kanaya, Y., and Wang, Z.: Technical Note: Determination of formaldehyde mixing ratios in air with PTR-MS: laboratory experiments and field measurements, Atmos. Chem. Phys., 8, 273–284, doi:10.5194/acp-8-273-2008, 2008. 3985, 4015
Irie, H., Kanaya, Y., Akimoto, H., Tanimoto, H., Wang, Z., Gleason, J. F., and Bucsela, E. J.: Validation of OMI tropospheric NO_2 column data using MAX-DOAS measurements deep inside the North China Plain in June 2006: Mount Tai Experiment 2006, Atmos. Chem. Phys., 8, 6577–6586, doi:10.5194/acp-8-6577-2008, 2008. 3985, 3995, 3997, 4015
Irie, H., Takashima, H., Kanaya, Y., Boersma, K. F., Gast, L., Wittrock, F., Brunner, D., Zhou, Y., and Van Roozendael, M.: Eight-component retrievals from ground-based MAX-DOAS observations, Atmos. Meas. Tech., 4, 1027–1044, doi:10.5194/amt-4-1027-2011, 2011. 3984, 3985, 4015, 4018
Jing, L. H., Steinberg, S. M., and Johnson, B. J.: Aldehyde and monocyclic aromatic hydrocarbon mixing ratios at an urban site in Las Vegas, Nevada, J. Air Waste Manage., 51, 1359–1366, 2001. 4002, 4018
Junkermann, W.: On the distribution of formaldehyde in the western Po-Valley, Italy, during FORMAT 2002/2003, Atmos. Chem. Phys., 9, 9187–9196, doi:10.5194/acp-9-9187-2009,

ACPD
12, 3983–4029, 2012

2009. 3990
Kawamura, K., Steinberg, S., and Kaplan, I. R.: Homologous series of C_1–C_{10} monocarboxylic acids and C_1–C_6 carbonyls in Los Angeles air and motor vehicle exhausts, Atmos. Environ., 34, 4175–4191, 2000. 4018
Klippel, T., Fischer, H., Bozem, H., Lawrence, M. G., Butler, T., Jöckel, P., Tost, H., Martinez, M., Harder, H., Regelin, E., Sander, R., Schiller, C. L., Stickler, A., and Lelieveld, J.: Distribution of hydrogen peroxide and formaldehyde over Central Europe during the HOOVER project, Atmos. Chem. Phys., 11, 4391–4410, doi:10.5194/acp-11-4391-2011, 2011. 3990
Kurucz, R. L., Furenlid, I., J., and Testerman, L.: Solar Flux Atlas from 296 to 1300 nm, Technical report, National Solar Observatory, 1984. 3989
Lee, Y.-N., Zhou, X., and Hallock, K.: Atmospheric carbonyl compounds at a rural Southeastern United States site, J. Geophys. Res., 100, 25933–25944, doi:10.1029/95jd02605, 1995. 4001, 4018
Lee, Y. N., Zhou, X., Kleinman, L. I., Nunnermacker, L. J., Springston, S. R., Daum, P. H., Newman, L., Keigley, W. G., Holdren, M. W., Spicer, C. W., Young, V., Fu, B., Parrish, D. D., Holloway, J., Williams, J., Roberts, J. M., Ryerson, T. B., and Fehsenfeld, F. C.: Atmospheric chemistry and distribution of formaldehyde and several multioxygenated carbonyl compounds during the 1995 Nashville/Middle Tennessee Ozone Study, J. Geophys. Res., 103, 22449–22462, doi:10.1029/98jd01251, 1998. 4018
Lei, W., Zavala, M., de Foy, B., Volkamer, R., Molina, M. J., and Molina, L. T.: Impact of primary formaldehyde on air pollution in the Mexico City Metropolitan Area, Atmos. Chem. Phys., 9, 2607–2618, doi:10.5194/acp-9-2607-2009, 2009. 4000, 4002, 4018
Leser, H., Hönninger, G., and Platt, U.: MAX-DOAS measurements of BrO and NO_2 in the marine boundary layer, Geophys. Res. Lett., 30, 1537, doi:10.1029/2002gl015811, 2003. 3985, 4015
Li, X., Brauers, T., Shao, M., Garland, R. M., Wagner, T., Deutschmann, T., and Wahner, A.: MAX-DOAS measurements in southern China: retrieval of aerosol extinctions and validation using ground-based in-situ data, Atmos. Chem. Phys., 10, 2079–2089, doi:10.5194/acp-10-2079-2010, 2010. 3986, 3987, 3989, 3991, 3992, 3993, 3995, 3996, 4016
Li, X., Brauers, T., Häseler, R., Bohn, B., Hofzumahaus, A., Holland, F., Lu, K. D., Rohrer, F., Hu, M., Zeng, L. M., Zhang, Y. H., Garland, R., Su, H., Nowak, A., Takegawa, N., Shao, M., and Wahner, A.: Exploring the atmospheric chemistry of nitrous acid (HONO) at a rural site in Southern China, Atmos. Chem. Phys. Discuss., 11, 27591–27635, doi:10.5194/acpd-11-

ACPD
12, 3983–4029, 2012

MAX-DOAS trace gases measurements in China

X. Li et al.

27591-2011, 2011. 3987
Liu, W., Zhang, J., Kwon, J., Weisel, C., Turpin, B., Zhang, L., Korn, L., Morandi, M., Stock, T., and Colome, S.: Concentrations and source characteristics of airborne carbonyl compounds measured outside urban residences, J. Air Waste Manage., 56, 1196–1204, 2006. 4002, 4018
Lou, S., Holland, F., Rohrer, F., Lu, K., Bohn, B., Brauers, T., Chang, C. C., Fuchs, H., Häseler, R., Kita, K., Kondo, Y., Li, X., Shao, M., Zeng, L., Wahner, A., Zhang, Y., Wang, W., and Hofzumahaus, A.: Atmospheric OH reactivities in the Pearl River Delta – China in summer 2006: measurement and model results, Atmos. Chem. Phys., 10, 11243–11260, doi:10.5194/acp-10-11243-2010, 2010. 3987, 3998, 3999
Lu, K. D., Rohrer, F., Holland, F., Fuchs, H., Bohn, B., Brauers, T., Chang, C. C., Häseler, R., Hu, M., Kita, K., Kondo, Y., Li, X., Lou, S. R., Nehr, S., Shao, M., Zeng, L. M., Wahner, A., Zhang, Y. H., and Hofzumahaus, A.: Observation and modelling of OH and HO_2 concentrations in the Pearl River Delta 2006: a missing OH source in a VOC rich atmosphere, Atmos. Chem. Phys. Discuss., 11, 11311–11378, doi:10.5194/acpd-11-11311-2011, 2011. 3987, 4000, 4002
Meller, R. and Moortgat, G. K.: Temperature dependence of the absorption cross sections of formaldehyde between 223 and 323 K in the wavelength range 225–375 nm, J. Geophys. Res., 105, 7089–7101, doi:10.1029/1999jd901074, 2000. 3988
Moortgat, G. K., Grossmann, D., Boddenberg, A., Dallmann, G., Ligon, A. P., Turner, W. V., Gäb, S., Slemr, F., Wieprecht, W., Acker, K., Kibler, M., Schlomski, S., and Bächmann, K.: Hydrogen peroxide, organic peroxides and higher carbonyl compounds determined during the BERLIOZ campaign, J. Atmos. Chem., 42, 443–463, doi:10.1023/A:1015743013107, 2002. 4018
Müller, K., Haferkorn, S., Grabmer, W., Wisthaler, A., Hansel, A., Kreuzwieser, J., Cojocariu, C., Rennenberg, H., and Herrmann, H.: Biogenic carbonyl compounds within and above a coniferous forest in Germany, Atmos. Environ., 40, 81–91, doi:10.1016/j.atmosenv.2005.10.070, 2006. 4018
Munger, J. W., Jacob, D. J., Daube, B. C., Horowitz, L. W., Keene, W. C., and Heikes, B. G.: Formaldehyde, glyoxal, and methylglyoxal in air and cloudwater at a rural mountain site in Central Virginia, J. Geophys. Res., 100, 9325–9333, doi:10.1029/95JD00508, 1995. 4000, 4001, 4018
Myriokefalitakis, S., Vrekoussis, M., Tsigaridis, K., Wittrock, F., Richter, A., Brühl, C.,

ACPD
12, 3983–4029, 2012

Volkamer, R., Burrows, J. P., and Kanakidou, M.: The influence of natural and anthropogenic secondary sources on the glyoxal global distribution, Atmos. Chem. Phys., 8, 4965–4981, doi:10.5194/acp-8-4965-2008, 2008. 3999

Pikelnaya, O., Hurlock, S. C., Trick, S., and Stutz, J.: Intercomparison of multiaxis and long-path differential optical absorption spectroscopy measurements in the marine boundary layer, J. Geophys. Res., 112, D10S01, doi:10.1029/2006jd007727, 2007. 3985, 3995, 4015

Platt, U., Marquard, L., Wagner, T., and Perner, D.: Corrections for zenith scattered light DOAS, Geophys. Res. Lett., 24, 1759–1762, doi:10.1029/97gl01693, 1997. 3989

Possanzini, M., Tagliacozzo, G., and Cecinato, A.: Ambient levels and sources of lower carbonyls at Montelibretti, Rome (Italy), Water Air Soil Poll., 183, 447–454, doi:10.1007/s11270-007-9393-1, 2007. 4002, 4018

Press, W. H., Teukolsky, S. A., Vetterling, W. T., and Flannery, B. P. (Eds.): Modeling of data, chap. 15, in: Numerical Recipes – The Art of Scientific Computing, 3rd edn., Cambridge University Press, The Edinburgh Building, Cambridge CB2 8RU, UK, 773–815, 2007. 3995

Richter, A., Burrows, J. P., Nusz, H., Granier, C., and Niemeier, U.: Increase in tropospheric nitrogen dioxide over China observed from space, Nature, 437, 129–132, doi:10.1038/nature04092, 2005. 3986

Rodgers, C. D.: Inverse Methods for Atmospheric Sounding: Theory and Practice, vol. 2 of Atmospheric, Oceanic and Planetary Physics, World Scientific, Hackensack, NJ, 2000. 3985

Rothman, L. S., Jacquemart, D., Barbe, A., Chris Benner, D., Birk, M., Brown, L. R., Carleer, M. R., Chackerian, J. C., Chance, K., Coudert, L. H., Dana, V., Devi, V. M., Flaud, J. M., Gamache, R. R., Goldman, A., Hartmann, J. M., Jucks, K. W., Maki, A. G., Mandin, J. Y., Massie, S. T., Orphal, J., Perrin, A., Rinsland, C. P., Smith, M. A. H., Tennyson, J., Tolchenov, R. N., Toth, R. A., Vander Auwera, J., Varanasi, P., and Wagner, G.: The HITRAN 2004 molecular spectroscopic database, J. Quant. Spectrosc. Ra., 96, 139–204, doi:10.1016/j.jqsrt.2004.10.008, 2005. 3988

Schauer, J. J., Kleeman, M. J., Cass, G. R., and Simoneit, B. R. T.: Measurement of emissions from air pollution sources. 2. C_1 through C_{30} organic compounds from medium duty diesel trucks, Environ. Sci. Technol., 33, 1578–1587, doi:10.1021/es980081n, 1999. 4001

Schauer, J. J., Kleeman, M. J., Cass, G. R., and Simoneit, B. R. T.: Measurement of Emissions from Air Pollution Sources. 3. C_1–C_{29} organic compounds from fireplace combustion of wood, Environ. Sci. Technol., 35, 1716–1728, doi:10.1021/es001331e, 2001. 4001

Schauer, J. J., Kleeman, M. J., Cass, G. R., and Simoneit, B. R. T.: Measurement of emissions

ACPD
12, 3983–4029, 2012

from air pollution sources. 5. C_1–C_{32} organic compounds from gasoline-powered motor vehicles, Environ. Sci. Technol., 36, 1169–1180, doi:10.1021/es0108077, 2002. 4001

Sinreich, R., Volkamer, R., Filsinger, F., Frieß, U., Kern, C., Platt, U., Sebastián, O., and Wagner, T.: MAX-DOAS detection of glyoxal during ICARTT 2004, Atmos. Chem. Phys., 7, 1293–1303, doi:10.5194/acp-7-1293-2007, 2007. 4015

Takegawa, N., Miyakawa, T., Kondo, Y., Jimenez, J. L., Zhang, Q., Worsnop, D. R., and Fukuda, M.: Seasonal and diurnal variations of submicron organic aerosol in Tokyo observed using the Aerodyne aerosol mass spectrometer, J. Geophys. Res., 111, D11206, doi:10.1029/2005jd006515, 2006. 3992

Theys, N., Van Roozendael, M., Hendrick, F., Fayt, C., Hermans, C., Baray, J.-L., Goutail, F., Pommereau, J.-P., and De Mazière, M.: Retrieval of stratospheric and tropospheric BrO columns from multi-axis DOAS measurements at Reunion Island (21° S, 56° E), Atmos. Chem. Phys., 7, 4733–4749, doi:10.5194/acp-7-4733-2007, 2007. 4015

Voigt, S., Orphal, J., Bogumil, K., and Burrows, J. P.: The temperature dependence (203–293 K) of the absorption cross sections of O_3 in the 230–850 nm region measured by Fourier-transform spectroscopy, J. Photoch. Photobio. A, 143, 1–9, doi:10.1016/s1010-6030(01)00480-4, 2001. 3988

Voigt, S., Orphal, J., and Burrows, J. P.: The temperature and pressure dependence of the absorption cross-sections of NO_2 in the 250–800 nm region measured by Fourier-transform spectroscopy, J. Photoch. Photobio. A, 149, 1–7, doi:10.1016/s1010-6030(01)00650-5, 2002. 3988

Volkamer, R., Spietz, P., Burrows, J., and Platt, U.: High-resolution absorption cross-section of glyoxal in the UV-vis and IR spectral ranges, J. Photoch. Photobio. A, 172, 35–46, doi:10.1016/j.jphotochem.2004.11.011, 2005. 3988

Vrekoussis, M., Wittrock, F., Richter, A., and Burrows, J. P.: Temporal and spatial variability of glyoxal as observed from space, Atmos. Chem. Phys., 9, 4485–4504, doi:10.5194/acp-9-4485-2009, 2009. 3986, 3999

Vrekoussis, M., Wittrock, F., Richter, A., and Burrows, J. P.: GOME-2 observations of oxygenated VOCs: what can we learn from the ratio glyoxal to formaldehyde on a global scale?, Atmos. Chem. Phys., 10, 10145–10160, doi:10.5194/acp-10-10145-2010, 2010. 4001, 4002, 4003

Wagner, T., Burrows, J. P., Deutschmann, T., Dix, B., von Friedeburg, C., Frieß, U., Hendrick, F., Heue, K.-P., Irie, H., Iwabuchi, H., Kanaya, Y., Keller, J., McLinden, C. A., Oetjen, H.,

ACPD
12, 3983–4029, 2012

MAX-DOAS trace gases measurements in China

X. Li et al.

Palazzi, E., Petritoli, A., Platt, U., Postylyakov, O., Pukite, J., Richter, A., van Roozendael, M., Rozanov, A., Rozanov, V., Sinreich, R., Sanghavi, S., and Wittrock, F.: Comparison of box-air-mass-factors and radiances for Multiple-Axis Differential Optical Absorption Spectroscopy (MAX-DOAS) geometries calculated from different UV/visible radiative transfer models, Atmos. Chem. Phys., 7, 1809–1833, doi:10.5194/acp-7-1809-2007, 2007. 3991

Wagner, T., Beirle, S., Brauers, T., Deutschmann, T., Frieß, U., Hak, C., Halla, J. D., Heue, K. P., Junkermann, W., Li, X., Platt, U., and Pundt-Gruber, I.: Inversion of tropospheric profiles of aerosol extinction and HCHO and NO_2 mixing ratios from MAX-DOAS observations in Milano during the summer of 2003 and comparison with independent data sets, Atmos. Meas. Tech., 4, 2685–2715, doi:10.5194/amt-4-2685-2011, 2011. 3984, 3985, 3988, 3995, 4015

Wang, X., Zhang, Y., Hu, Y., Zhou, W., Lu, K., Zhong, L., Zeng, L., Shao, M., Hu, M., and Russell, A. G.: Process analysis and sensitivity study of regional ozone formation over the Pearl River Delta, China, during the PRIDE-PRD2004 campaign using the Community Multiscale Air Quality modeling system, Atmos. Chem. Phys., 10, 4423–4437, doi:10.5194/acp-10-4423-2010, 2010. 3992

Wilmouth, D. M., Hanisco, T. F., Donahue, N. M., and Anderson, J. G.: Fourier transform ultraviolet spectroscopy of the $A^2\Pi_{3/2} \leftarrow X^2\Pi_{3/2}$ transition of BrO, J. Phys. Chem. A, 103, 8935–8945, doi:10.1021/jp991651o, 1999. 3988

Wittrock, F., Oetjen, H., Richter, A., Fietkau, S., Medeke, T., Rozanov, A., and Burrows, J. P.: MAX-DOAS measurements of atmospheric trace gases in Ny-Ålesund – Radiative transfer studies and their application, Atmos. Chem. Phys., 4, 955–966, doi:10.5194/acp-4-955-2004, 2004. 4015

Wittrock, F., Richter, A., Oetjen, H., Burrows, J. P., Kanakidou, M., Myriokefalitakis, S., Volkamer, R., Beirle, S., Platt, U., and Wagner, T.: Simultaneous global observations of glyoxal and formaldehyde from space, Geophys. Res. Lett., 33, L16804, doi:10.1029/2006gl026310, 2006. 3986

Xiao, R., Takegawa, N., Zheng, M., Kondo, Y., Miyazaki, Y., Miyakawa, T., Hu, M., Shao, M., Zeng, L., Gong, Y., Lu, K., Deng, Z., Zhao, Y., and Zhang, Y. H.: Characterization and source apportionment of submicron aerosol with aerosol mass spectrometer during the PRIDE-PRD 2006 campaign, Atmos. Chem. Phys., 11, 6911–6929, doi:10.5194/acp-11-6911-2011, 2011. 3987

Yue, D. L., Hu, M., Wu, Z. J., Guo, S., Wen, M. T., Nowak, A., Wehner, B., Wiedensohler, A., Takegawa, N., Kondo, Y., Wang, X. S., Li, Y. P., Zeng, L. M., and Zhang, Y. H.: Variation of particle number size distributions and chemical compositions at the urban and downwind regional sites in the Pearl River Delta during summertime pollution episodes, Atmos. Chem. Phys., 10, 9431–9439, doi:10.5194/acp-10-9431-2010, 2010. 3987

Zhang, Y. H., Hu, M., Shao, M., Brauers, T., Chang, C. C., Hofzumahaus, A., Holland, F., Li, X., Lu, K., Kita, K., Kondo, Y., Nowak, A., Pöschl, U., Rohrer, F., Zeng, L., Wiedensohler, A., and Wahner, A.: Continuous efforts to investigate regional air pollution in the Pearl River Delta, China: PRIDE-PRD2006 campaign, Atmos. Chem. Phys. Discuss., in preparation, 2012. 3986

Zheng, J., Zhang, L., Che, W., Zheng, Z., and Yin, S.: A highly resolved temporal and spatial air pollutant emission inventory for the Pearl River Delta region, China and its uncertainty assessment, Atmos. Environ., 43, 5112–5122, doi:10.1016/j.atmosenv.2009.04.060, 2009. 3993

Zhou, X. and Mopper, K.: Apparent partition coefficients of 15 carbonyl compounds between air and seawater and between air and freshwater; implications for air-sea exchange, Environ. Sci. Technol., 24, 1864–1869, doi:10.1021/es00082a013, 1990. 4018

Table 1. Overview of MAX-DOAS trace gas measurements.

Location	Period	# [a]	Species	RTM	Methodology	Ref.
Alert, Canada	Apr–May 2000	6	BrO	–	Geometric approach	1
Atlantic Ocean	Oct 2000	6	NO_2, BrO	–	Geometric approach	2
Montserrat island	May 2002	10	SO_2, BrO	–	Geometric approach	3
Ny-Ålesund Svalbard	Jul 2002	5	NO_2	SCIATRAN	Predefined trace gas profile + RTM calculation	4
Po-valley, Italy	Sep 2003	5	HCHO	SCIATRAN	Manual iteration method	5
Cambridge & Gulf of Maine, USA	Jul–Aug 2004	5	NO_2, HCHO, CHOCHO	TRACY	Manual iteration method	6
Reunion Island	Aug 2004–Jun 2005	5	BrO	DISORT	Predefined profiles + OEM[b]	7
Mount Tai, China	Jun 2006	5	HCHO, NO_2	MCARaTS	Parametrized profile + OEM	8
Cabauw, Netherlands	Jun–Jul 2009	6	SO_2, HCHO, NO_2, CHOCHO	MCARaTS	Parametrized profile + OEM	9
Po-valley, Italy	Sep 2003	5	HCHO, NO_2	McArtim	Parametrized profile + LMA[c]	10
Pearl River Delta, China	Jul 2006	7	NO_2, HCHO, CHOCHO	McArtim	Parametrized profile + LMA	11

[a] Number of elevation angles, [b] Optimal Estimation Method, [c] Levenberg-Marquardt Algorithm
[1] Hönninger and Platt (2002), [2] Leser et al. (2003), [3] Bobrowski et al. (2003) [4] Wittrock et al. (2004), [5] Heckel et al. (2005), [6] Pikelnaya et al. (2007); Sinreich et al. (2007), [7] Theys et al. (2007), [8] Inomata et al. (2008); Irie et al. (2008), [9] Irie et al. (2011), [10] Wagner et al. (2011), [11] this work.

Table 2. Parameter settings of RTM calculations for NO_2, HCHO, and CHOCHO DSCDs.

Parameter	Value		
	NO_2	HCHO	CHOCHO
Wavelength	435 nm	339 nm	440 nm
Surface albedo	7 %		
Single scattering albedo (SSA)	0.85		
Asymmetry factor (g)	0.68		
Aerosol profile	from O_4 DSCDs at 360 nm[a]		
O_3 profile	USSA[b] filled with 40 ppb from 0–1 km		
T and *P* profiles	USSA		
NO_2 profile	0–15 km: from NO_2 DSCDs at 435 nm > 15 km: USSA		

[a] see Li et al. (2010)
[b] US Standard atmosphere

ACPD
12, 3983–4029, 2012

Table 3. Sensitivities of the RTM inputs on the calculated NO_2, HCHO, and CHOCHO DSCDs.

	Surface albedo	FOV	SSA	g	AOD	NO_2 (≤ 1 km)	O_3 (≤ 1 km)
Δ Param.	× 2	± 0.1°	10 %	10 %	× 3	× 10	× 5
Δ DSCDs							
NO_2	2.4 %	0.4 %	7.6 %	9.3 %	47.7 %	–	0.03 %
HCHO	1.7 %	0.5 %	6.7 %	9.1 %	49.5 %	0.04 %	4.6 %
CHOCHO	1.7 %	0.3 %	7.6 %	10.9 %	49.3 %	0.01 %	5.4 %

ACPD
12, 3983–4029, 2012

Table 4. Overview of mean values of HCHO and CHOCHO mixing ratios (unit: ppb) and R_{GF} in different environments in the world. Results shown here are in conditions that simultaneous HCHO and CHOCHO measurements are available.

Location	Site	Period	HCHO	CHOCHO	R_{GF}	Reference
Caribbean Sea and Sargasso Sea	Marine	Autumn, Spring	0.4	0.08	0.200	Zhou and Mopper (1990)
Metter, Georgia, USA	Rural	Summer	3.6	0.02	0.006	Lee et al. (1995)
Pinnacles, Virginia, USA	Rural	Autumn	0.98	0.04	0.045	Munger et al. (1995)
San Nicolas, USA	Rural	Autumn	0.8	0.1	0.132	Grosjean et al. (1996)
Nashvile, USA	Rural	Summer	4.2	0.07	0.017	Lee et al. (1998)
Giesta, Portugal	Rural	Summer	6.14	1.54	0.251	Borrego et al. (2000)
Pabstthum, Germany	Rural	Summer	2.58	0.03	0.012	Moortgat et al. (2002)
Anadia, Portugal	Rural	Summer	1.8	0.08	0.044	Cerqueira et al. (2003)
Goldlauter, Germany	Rural	Autumn	0.75	0.04	0.058	Müller et al. (2006)
Montelibretti, Italy	Rural	Summer	5.10	0.55	0.107	Possanzini et al. (2007)
		Autumn	3.38	0.22	0.064	
Sierra Nevada, USA	Rural	Autumn	6.88	0.03	0.004	Choi et al. (2010); Huisman et al. (2011)
Cabauw, Netherlands	Rural	Summer	2.5	0.08	0.036	Irie et al. (2011)
Sao Paulo, Barzil	Urban	Summer	10.4	0.7	0.092	Grosjean et al. (1990)
Los Angeles, USA	Urban	Summer	5.3	0.8	0.137	Grosjean et al. (1996)
	Urban	Autumn	1.0	0.3	0.300	Kawamura et al. (2000)
Las Vegas, USA	Urban	Summer	0.26	0.21	0.808	Jing et al. (2001)
		Winter	0.79	0.14	0.177	
Hongkong, China	Urban	–	11.3	1.5	0.122	Ho and Yu (2002)
Elizabeth, New Jersey, USA	Urban	Spring	5.29	0.72	0.136	Liu et al. (2006)
		Summer	3.86	0.71	0.183	
		Autumn	4.67	0.51	0.109	
		Winter	5.67	0.45	0.079	
Mexico City, Mexico	Urban	Spring	12.5	0.45	0.036	Lei et al. (2009)
Back Garden, China	Rural	Summer	11.8	1.6	0.135	This work

ACPD
12, 3983–4029, 2012

MAX-DOAS trace gases measurements in China

X. Li et al.

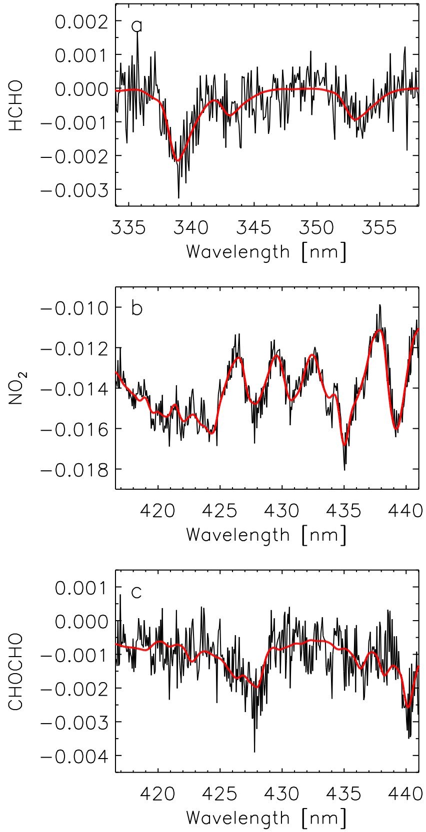

Fig. 1. Example of DOAS fit results for **(a)** HCHO, **(b)** NO_2, and **(c)** CHOCHO. The evaluated spectrum was recorded on 19 July 2006 at 10:59 LT, at $\alpha = 3^\circ$. Red line represents the fitted reference spectrum. Black line is the fit residual plus the absorption of the target species. Detailed settings of the DOAS fit are listed in Table S1 in the Supplement.

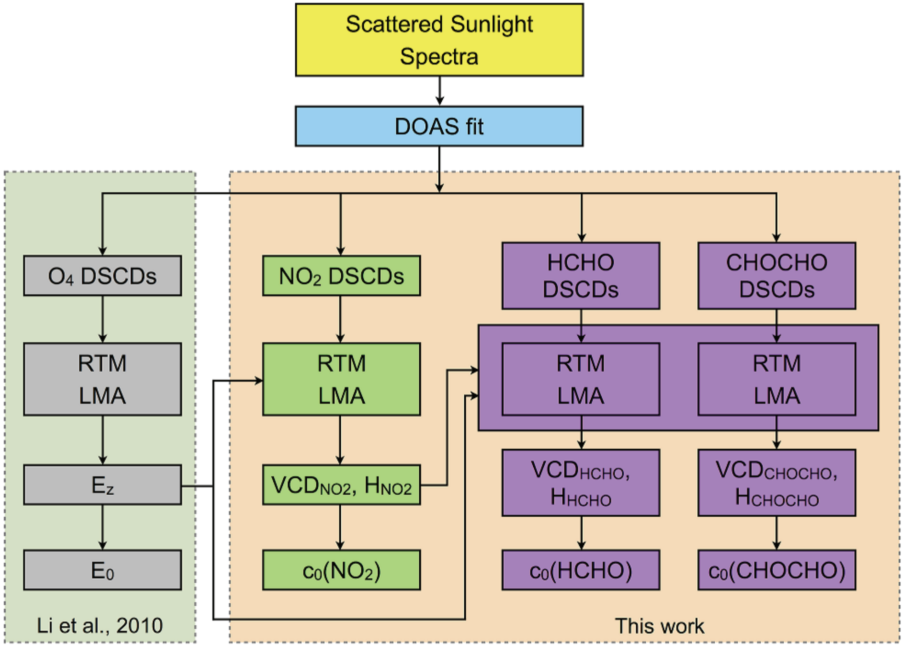

Fig. 2. Flow diagram of MAX-DOAS trace gas vertical distribution retrieval.

ACPD
12, 3983–4029, 2012

MAX-DOAS trace gases measurements in China

X. Li et al.

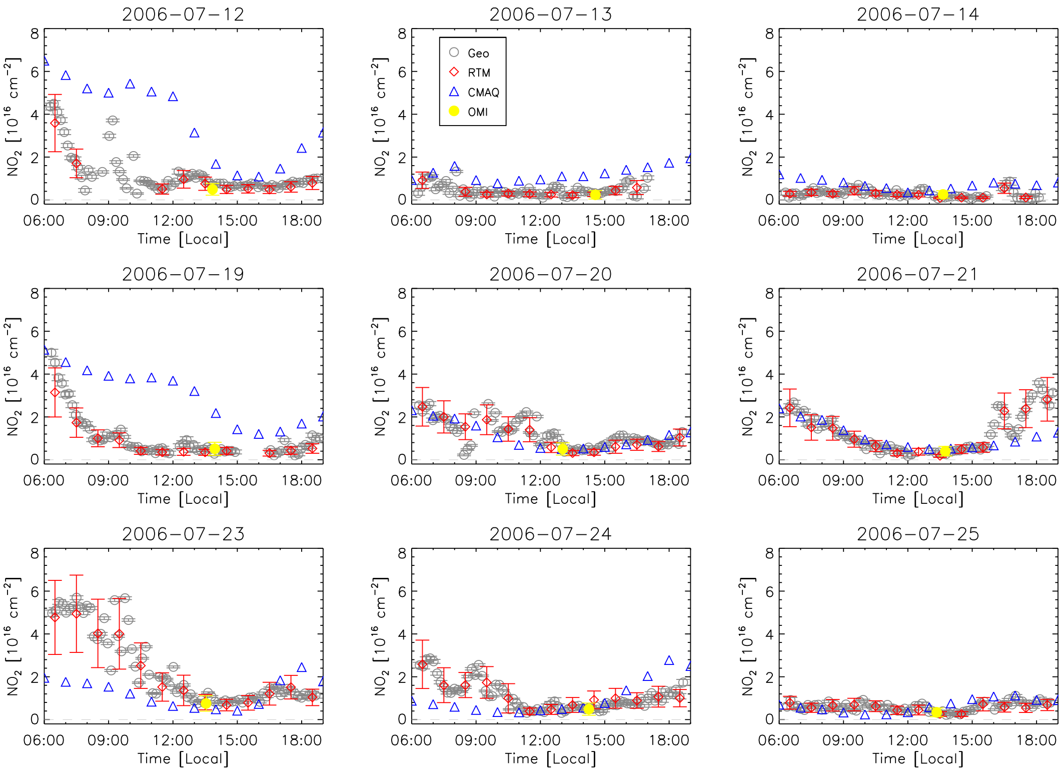

Fig. 3. Time series of NO_2 vertical column densities (VCDs) in the 9 cloud-free days during the PRIDE-PRD2006 campaign. The grey circles represent NO_2 VCDs calculated by the geometric approach (i.e. Eq. 1), the red diamonds refer to NO_2 VCDs derived from the NO_2 vertical distribution retrieval (i.e. Fig. 2), the blue triangles are NO_2 VCDs calculated by the CMAQ model, and the yellow dots are NO_2 VCDs observed by OMI from space.

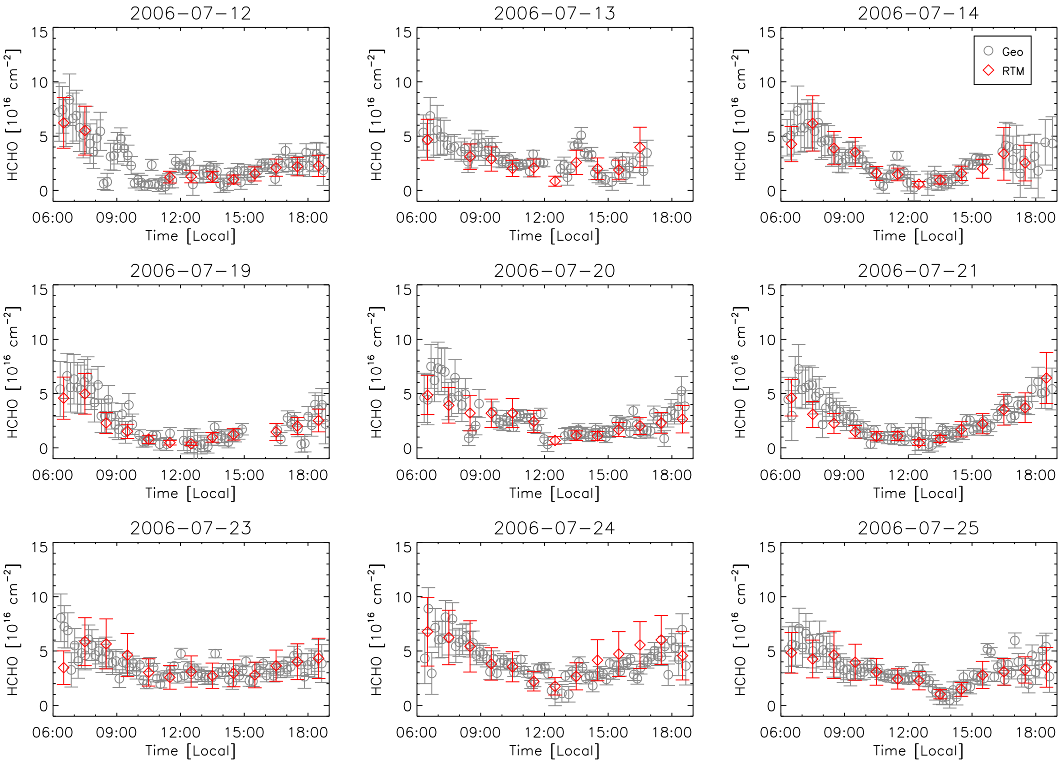

Fig. 4. Time series of HCHO vertical column densities (VCDs) in the 9 cloud-free days during the PRIDE-PRD2006 campaign. The grey circles represent HCHO VCDs calculated by the geometric approach (i.e. Eq. 1), and the red diamonds refer to HCHO VCDs derived from the HCHO vertical distribution retrieval (i.e. Fig. 2).

ACPD
12, 3983–4029, 2012

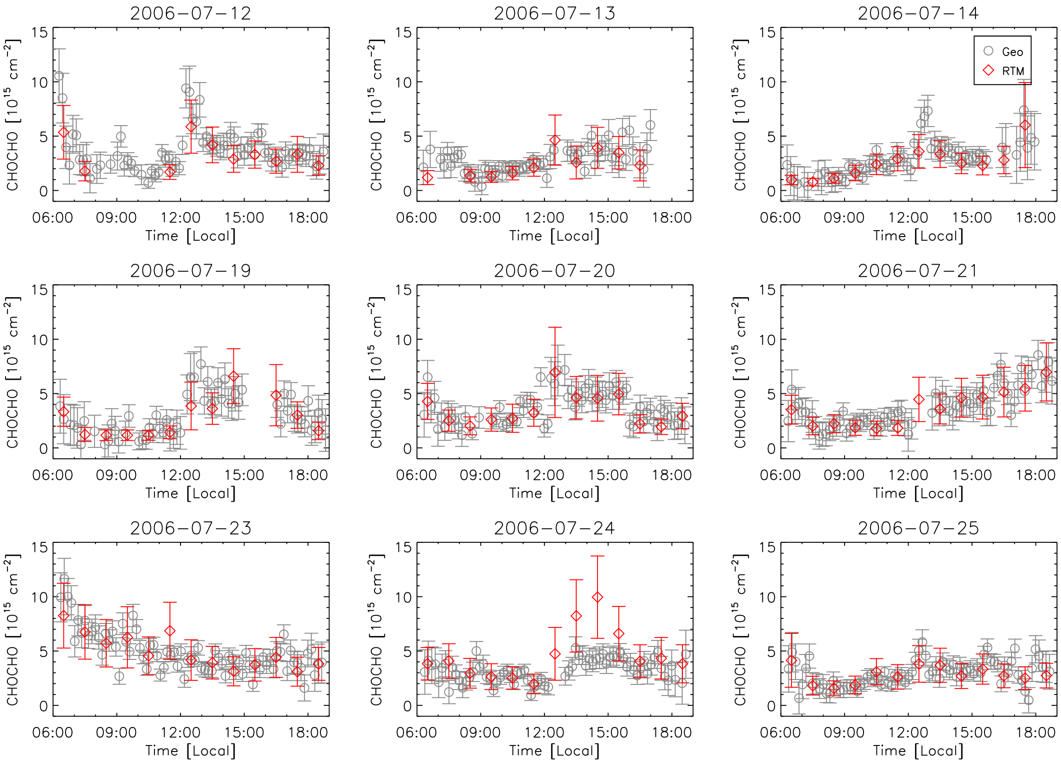

Fig. 5. Time series of CHOCHO vertical column densities (VCDs) in the 9 cloud-free days during the PRIDE-PRD2006 campaign. The grey circles represent CHOCHO VCDs calculated by the geometric approach (i.e. Eq. 1), and the red diamonds refer to CHOCHO VCDs derived from the CHOCHO vertical distribution retrieval (i.e. Fig. 2).

ACPD
12, 3983–4029, 2012

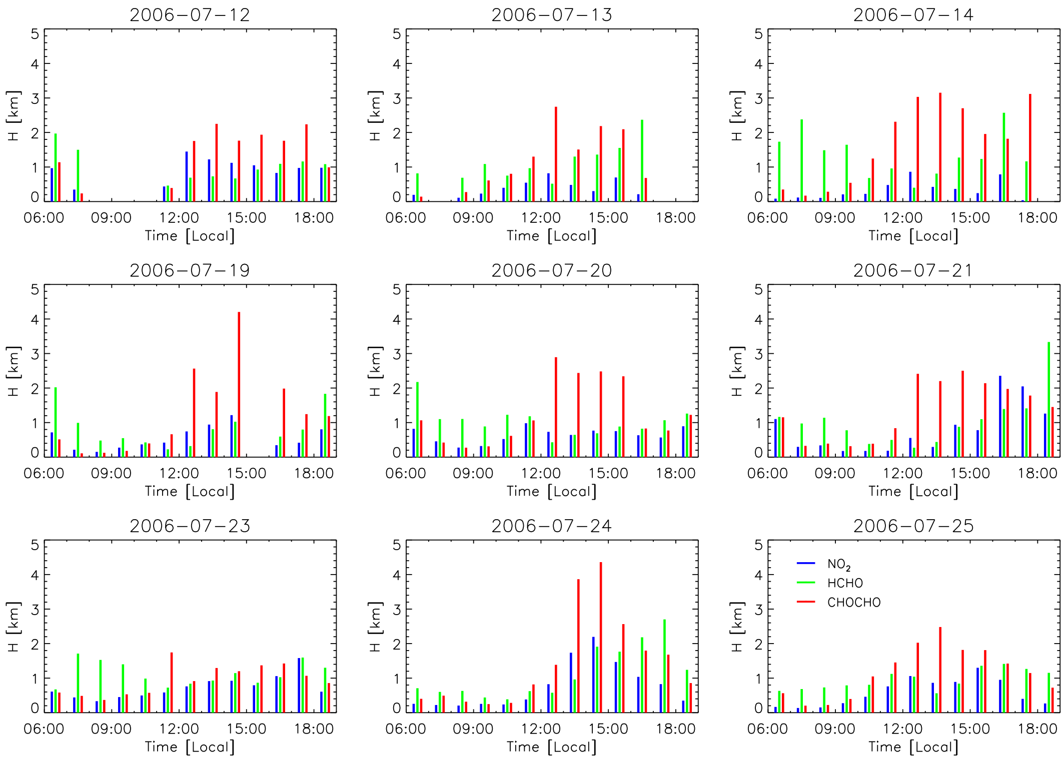

Fig. 6. Time series of mixed layer heights of NO_2, HCHO, and CHOCHO in the 9 cloud-free days during the PRIDE-PRD2006 campaign.

ACPD
12, 3983–4029, 2012

MAX-DOAS trace gases measurements in China

X. Li et al.

Title Page
Abstract | Introduction
Conclusions | References
Tables | Figures
◀| |▶
◀ ▶
Back | Close
Full Screen / Esc
Printer-friendly Version
Interactive Discussion

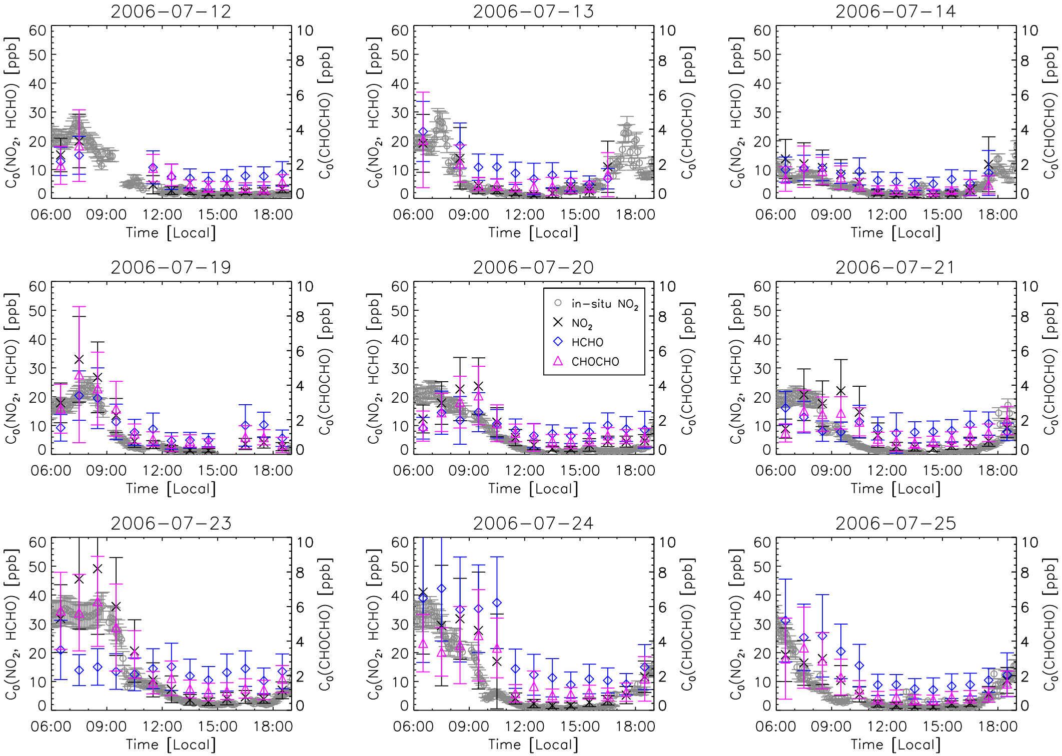

Fig. 7. Time series of NO_2 (black cross), HCHO (blue diamond), and CHOCHO (pink triangle) mixing ratios near the ground surface derived from the MAX-DOAS measurements, and NO_2 mixing ratios measured by in-situ chemiluminescence instrument (grey circle) in the 9 cloud-free days during the PRIDE-PRD2006 campaign.

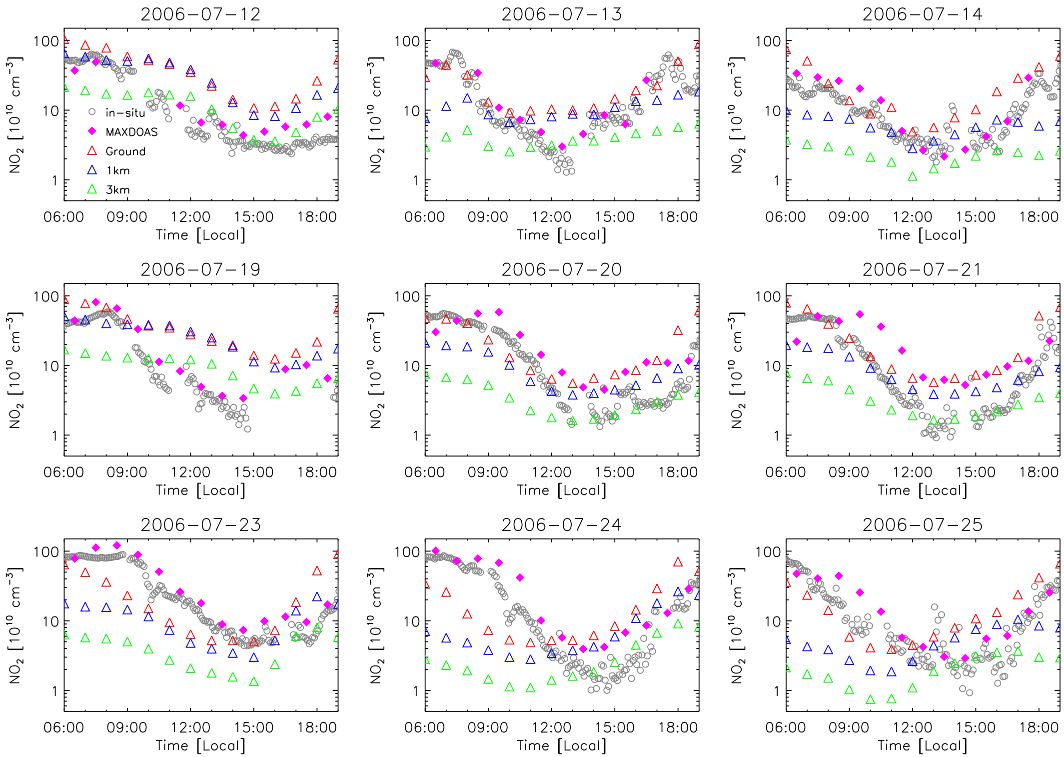

Fig. 8. Time series of NO_2 concentrations measured by MAX-DOAS (full pink diamond) and in-situ chemiluminescence instrument (open grey circle), and simulated by the CMAQ model in the 9 cloud-free days during the PRIDE-PRD2006 campaign. The "ground" (open red triangle), "1 km" (blue triangle), and "3 km" (open green triangle) represent the average NO_2 concentrations calculated by the CMAQ model in the layer of 0–18 m, 0–1 km, and 0–3 km, respectively.

ACPD

12, 3983–4029, 2012

MAX-DOAS trace gases measurements in China

X. Li et al.

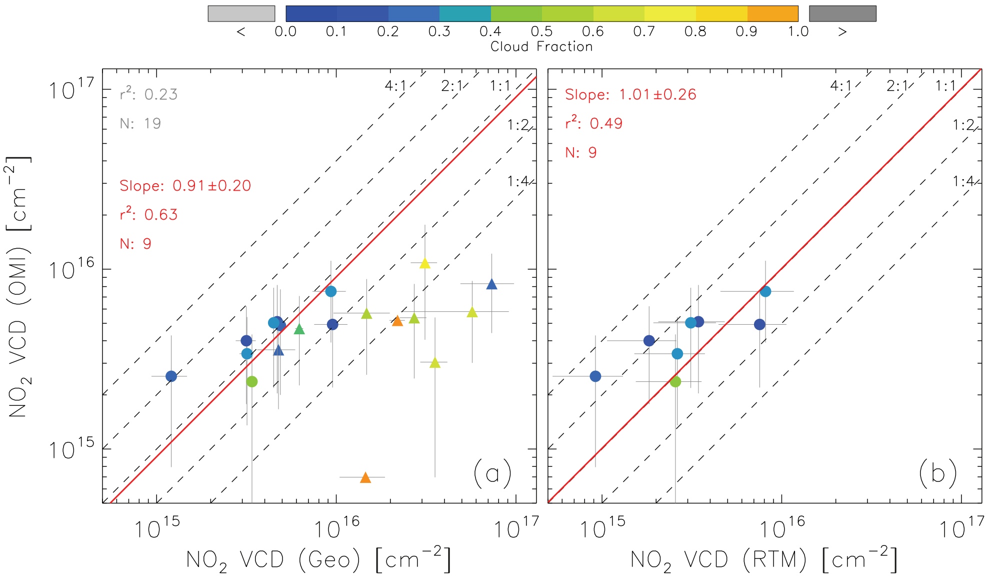

Fig. 9. Comparison of tropospheric NO_2 VCDs derived from MAX-DOAS and OMI observations during the PRIDE-PRD2006 campaign. The x-axis in **(a)** and **(b)** corresponds to the NO_2 VCDs derived from the geometric approach and the NO_2 vertical distribution retrieval, respectively. The dots represent data obtained in the 9 cloud-free days. The regression and correlation results for the dots and triangles are shown in red and grey texts, respectively. The regression lines are forced to pass the origin during the regressions.

ACPD
12, 3983–4029, 2012

MAX-DOAS trace gases measurements in China

X. Li et al.

Title Page
Abstract | Introduction
Conclusions | References
Tables | Figures
◀| |▶
◀ ▶
Back | Close
Full Screen / Esc
Printer-friendly Version
Interactive Discussion

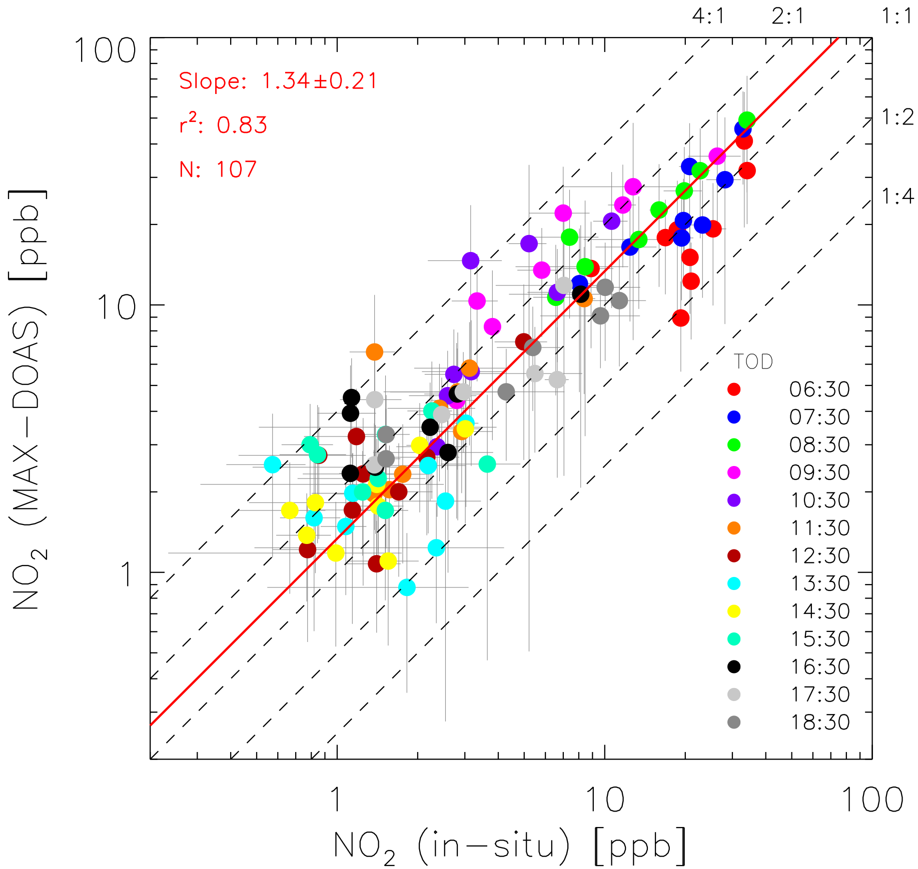

Fig. 10. Comparison of NO_2 mixing ratios measured by MAX-DOAS and in-situ chemiluminescence technique during the PRIDE-PRD2006 campaign. Data displayed here are obtained in the 9 cloud-free days. The regression line is forced to pass the origin during the regression.

ACPD
12, 3983–4029, 2012

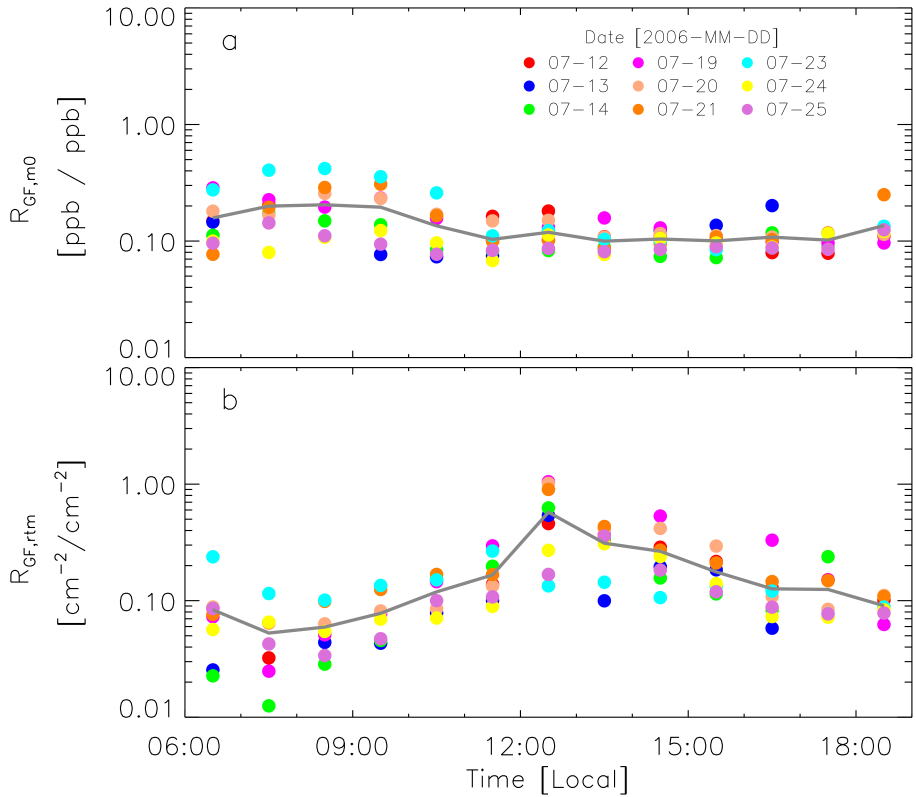

Fig. 11. Diurnal variation of CHOCHO/HCHO ratio (R_{GF}) in the 9 cloud-free days during the PRIDE-PRD2006 campaign. The dots are values calculated from individually measured m_0 (pannel **a**) and VCD_{rtm} (pannel **b**). Solid lines refer to the average values of the individual points.

ACPD
12, 3983–4029, 2012